Sonic hedgehog signaling in astrocytes mediates cell type-specific synaptic organization

AUTHORS: Steven Hill[1,§], Andrew S. Blaeser[1,§], Austin A. Coley[2], Yajun Xie[3], Katherine A. Shepard[1], Corey C. Harwell[3], Wen-Jun Gao[2], A. Denise R. Garcia[1,2*]

[1]Department of Biology, Drexel University, Philadelphia, PA 19104, USA
[2]Department of Neurobiology and Anatomy, Drexel University College of Medicine, Philadelphia, PA 19129, USA
[3]Department of Neurobiology, Harvard Medical School, Boston, MA 02115, USA
[§]Authors contributed equally to this work.

Correspondence:
A. Denise R. Garcia
Department of Biology
Department Neurobiology and Anatomy
Drexel University
3245 Chestnut St. PISB 422
Philadelphia, PA 19104
adg82@drexel.edu

ABSTRACT

Astrocytes have emerged as integral partners with neurons in regulating synapse formation and function, but the mechanisms that mediate these interactions are not well understood. Here, we show that Sonic hedgehog (Shh) signaling in mature astrocytes is required for establishing structural organization and remodeling of cortical synapses in a cell type-specific manner. In the postnatal cortex, Shh signaling is active in a subpopulation of mature astrocytes localized primarily in deep cortical layers. Selective disruption of Shh signaling in astrocytes produces a dramatic increase in synapse number specifically on layer V apical dendrites that emerges during adolescence and persists into adulthood. Dynamic turnover of dendritic spines is impaired in mutant mice and is accompanied by an increase in neuronal excitability and a reduction of the glial-specific, inward-rectifying K^+ channel Kir4.1. These data identify a critical role for Shh signaling in astrocyte-mediated modulation of neuronal activity required for sculpting synapses.

INTRODUCTION

The organization of synapses into the appropriate number and distribution occurs through a process of robust synapse addition followed by a period of refinement during which excess synapses are eliminated. Failure to establish or maintain appropriate synaptic organization is a hallmark of many neurodevelopmental disorders[1]. Considerable evidence now shows that, together with neurons, astrocytes are critical regulators of synaptic connectivity and function[2–4]. Astrocytes interact intimately with synapses to regulate their formation, maturation, and function, and a growing number of astrocyte-secreted proteins that directly mediate synapse formation and elimination have been identified[5–9]. In addition, astrocytes regulate concentrations of K^+ and glutamate in the extracellular space, thereby modulating neuronal activity[10]. Nevertheless, despite the remarkable progress in our understanding of the essential role for astrocytes in regulating synaptic formation and function, the underlying signaling programs mediating astrocyte-dependent regulation of synapse organization remain poorly understood.

The molecular signaling pathway Sonic hedgehog (Shh) governs a broad array of neurodevelopmental processes in the vertebrate embryo, including morphogenesis, cell proliferation and specification, and axon pathfinding[11,12]. However, Shh activity persists in multiple cell populations in the postnatal and adult CNS, including progenitor cells, as well as in differentiated neurons and astrocytes[13–17], where novel and unexpected roles for Shh activity are emerging[18]. Following injury, Shh has been shown to mitigate inflammation[19,20], and in the cerebellum, Shh derived from Purkinje neurons instructs phenotypic properties of mature Bergmann glia[21]. In the postnatal cortex, Shh is required for establishing local circuits between two distinct projection neuron populations[16]. Shh produced by layer V neurons guides the formation of synaptic connections to its layer II/III presynaptic partners, which transduce the Shh signal through non-canonical, Gli-independent mechanisms. We have previously shown that Shh signaling is also active in a discrete subpopulation of cortical astrocytes[17], suggesting that Shh signaling mediates both homotypic and heterotypic cellular interactions. Astrocytes engaging in Shh activity are identified by expression of Gli1, a transcriptional effector of canonical Shh signaling[11]. Whether Shh signaling in cortical astrocytes plays a role in synaptic organization of neurons is not known.

In this study, we examined the organization and dynamics of dendritic spines on cortical neurons following selective disruption of Shh signaling in astrocytes. Dendritic spines are the structural hosts of most excitatory synapses and play an important role in the organization and function of neural circuits. We show that deep layer neurons exhibit long-lasting aberrations in the density and turnover of dendritic spines that emerge during postnatal development following

71 selective disruption of Shh signaling in astrocytes. These perturbations in synaptic organization
72 are not observed in upper layer neurons where Gli1 astrocytes are relatively sparse. Chronic *in*
73 *vivo* imaging of dendritic spines reveals that mutant mice exhibit lower rates of spine turnover,
74 suggesting impaired structural plasticity. In addition, these mice show a pronounced deficit in
75 expression of the glial-specific inward-rectifying K^+ channel, Kir4.1, as well as an increase in
76 excitability of cortical neurons. Taken together, these data demonstrate that astrocytes act as
77 key modulators of neural activity and structure during postnatal development in a Shh-
78 dependent manner and further establish Shh signaling as a fundamental mediator of synaptic
79 connectivity.

80 RESULTS

81 Gli1 astrocytes exhibit a distinct laminar distribution in the adult cortex

82 In the mature cortex, a subpopulation of astrocytes express the transcription factor Gli1,
83 indicating active Shh signaling[17]. Notably, the distribution of Gli1 astrocytes throughout the
84 cortex is non-uniform, showing a laminar-specific pattern (**Figure 1**). We analyzed the laminar
85 distribution of Gli1 astrocytes in adult *Gli1*$^{CreER/+}$;Ai14 mice, in which tamoxifen administration
86 promotes Cre-mediated recombination of the fluorescent tdTomato reporter protein,
87 permanently marking Gli1-expressing cells. Adult *Gli1*$^{CreER/+}$;Ai14 mice received tamoxifen over
88 three days, and their brains were analyzed two – three weeks later. In our previous study, we
89 observed weak expression of βGal reporter protein in *Gli1*$^{CreER/+}$;*R26*$^{lacZ/lacZ}$ mice at time points
90 earlier than 4 weeks after tamoxifen[17]. In contrast, expression of the tdTomato reporter protein
91 in the Ai14 reporter line shows robust expression as early as two weeks, and a comparable
92 number, distribution and intensity of reporter-positive cells between two and four weeks[20]. For
93 these studies, we therefore used a two – three week chase after tamoxifen. The vast majority of
94 marked cells were observed within layers IV and V, with few marked cells observed in layers
95 II/III or VI (**Figure 1**). We performed immunostaining with the pan-astrocytic marker S100β and
96 quantified the fraction of marked astrocytes in cortical layers (**Figure 1**). This analysis showed
97 that 44% of astrocytes in layer IV express Gli1 (**Figure 1**), while 36% of astrocytes in layer V
98 express Gli1. Interestingly, the distribution of Gli1 astrocytes in layer V was not homogenous,
99 showing an enrichment of marked cells in layer Vb, and a distinctive paucity of marked cells in
100 layer Va (**Figure 1**), consistent with the localization of Shh producing neurons in layer Vb[16,17].
101 We analyzed the fraction of Gli1 astrocytes in each sublayer of layer V and found that 75% of
102 marked cells were found in layer Vb whereas only 25% were found in layer Va. Layers II/III and

103 VI showed the lowest fractions of marked astrocytes, with only 11% and 22% of S100β cells
104 expressing tomato, respectively. These data demonstrate that Gli1 astrocytes are preferentially
105 localized in deep cortical layers and suggest their interactions with local neurons may differ from
106 that of Gli1-negative astrocytes in superficial layers.

107 Shh signaling is required for cell type-specific synaptic connectivity

108 Transduction of canonical Shh signaling begins with binding of Shh to its
109 transmembrane receptor, Patched1 (Ptch), relieving inhibition of a second, obligatory co-
110 receptor Smoothened (Smo). To investigate the role of Shh signaling in astrocyte function, we
111 performed conditional knockout of Smo selectively in astrocytes using GFAP-Cre transgenic
112 mice in which Cre expression is regulated by the full-length mouse GFAP promoter[22] (mGFAP
113 Smo CKO). Because mGFAP-mediated Cre recombination targets astrocyte progenitors
114 expressing GFAP which are present at birth, this is an effective tool for targeting the cortical
115 astrocyte population for selective gene deletion. We validated the Cre-mediated recombination
116 pattern in mGFAP-Cre mice by crossing them with Ai14 reporter mice (*mGFAP-Cre;Ai14*), that
117 express the tdTomato reporter protein. Although individual floxed alleles possess distinct
118 recombination efficiencies, owing to specific characteristics of each allele including distance
119 between loxP sites or their accessibility due to chromatin structure[23], analysis of recombination
120 in a reporter line provides a useful approximation of the expression pattern of a given Cre driver.
121 We performed single cell analysis of the identity of recombined cells. The vast majority of
122 tomato-positive cells showed a bushy morphology, typical of protoplasmic astrocytes (**Figure 2**
123 **– figure supplement 1**). Single cell analysis of double staining with S100β showed that nearly
124 70% were co-labeled, identifying them as astrocytes. We also identified a small fraction (6%) of
125 tomato cells as oligodendrocytes. A small fraction (9%) of tomato cells were co-labeled with the
126 neuronal marker, NeuN, but this represented only 1.3% of cortical neurons (**Figure 2 – figure**
127 **supplement 1**). Importantly, although a minor fraction of recombined cells was identified as
128 neurons or oligodendrocytes, nearly all cortical astrocytes analyzed expressed the tdTomato
129 reporter protein (95%; **Figure 2 – figure supplement 1**), suggesting effective targeting of the
130 cortical astrocyte population using this mGFAP-Cre driver.
131 We performed qPCR on whole cortex from mGFAP Smo CKO mice and littermate
132 controls and found a 50% reduction in the number of Smo transcripts (**Figure 2 - figure**
133 **supplement 2**). As Smo is also expressed in neurons[16], the remaining Smo transcripts are
134 likely due to neurons that do not undergo Cre-mediated recombination in these mice.
135 Importantly, mGFAP Smo CKO mice show a nearly complete loss of Gli1 activity, with no

136 difference in the number of astrocytes in the mature cortex, demonstrating effective interruption
137 of canonical Shh signaling[17]. These data demonstrate that this mGFAP-Cre driver is an
138 effective tool for selective deletion of Smo in cortical astrocytes, and that canonical, Gli-
139 mediated Shh activity is effectively abolished

140 During postnatal development, Shh is required for establishing synaptic connectivity
141 between layer V neurons and their presynaptic partners in layer II/III, which is mediated by Gli-
142 independent, non-canonical signaling[16]. To examine whether canonical, Gli-mediated Shh
143 signaling in astrocytes plays a role in establishing synaptic connectivity of cortical neurons, we
144 evaluated spine density of apical dendrites on layer V neurons in the somatosensory cortex of
145 mGFAP Smo CKO mice across postnatal development. Dendritic spines receive the vast
146 majority of excitatory input, thereby serving as a useful readout of synaptic connectivity[24]. To
147 visualize neurons for reliable identification and tracing, mGFAP Smo CKO mice were crossed
148 with Thy1-GFPm transgenic mice, which sparsely express GFP in a subset of layer V cortical
149 neurons[25]. Dendritic spines undergo a period of dynamic reorganization during postnatal
150 development during which there is an initial overproduction of spines over the first 2-3 weeks of
151 postnatal development followed by a period of synaptic pruning that refines the precise
152 connectivity of cortical circuits[26]. At P14, spine density was comparable between mGFAP Smo
153 CKO mice and wild type (WT) littermate controls, suggesting that early synaptogenesis does not
154 require astrocytic Shh signaling (0.58 ± 0.03 spines/μm and 0.56 ± 0.01 spines/μm, WT [n = 7
155 cells] and mGFAP Smo CKO [n = 6 cells], respectively, p = 0.64, 2 animals per genotype).
156 Between P14 and P21, spine density remained stable in WT, but showed a dramatic increase at
157 P28 (**Figure 2**). This period of synapse addition was followed by a steady reduction in spine
158 density at P42 and into adulthood (≥P90), reflecting the developmental elimination of spines. In
159 contrast, mGFAP Smo CKO mice showed an accelerated timeline of spine addition in which
160 spine density increased dramatically between P14 and P21 (**Figure 2**). Spine density was
161 significantly higher at P21 in mGFAP Smo CKO mice compared to controls (0.53 ± 0.05
162 spines/μm and 0.76 ± 0.06 spines/μm, WT [n = 9 cells] and mGFAP Smo CKO [n = 9 cells],
163 respectively, p = 0.008, 3 animals per genotype). Although there was a modest reduction in
164 spine density as animals matured, spine density remained elevated in adult mGFAP Smo CKO
165 mice compared to WT controls (0.36 ± 0.02 spines/μm and 0.60 ± 0.02 spines/μm in WT [n = 24
166 cells] and mGFAP Smo CKO [n = 23 cells], respectively, $p < 0.0001$, 4 animals per genotype;
167 **Figure 2**). Thus, whereas WT mice experience a 49% reduction in spine density from the peak
168 of spine density at P28 to adulthood, mGFAP Smo CKO mice exhibit a 22% reduction from their
169 peak at P21 to adulthood. Interestingly, we find no difference in basal dendrite spine density in

170 mGFAP Smo CKO mice (0.60 ± 0.04 spines/um and 0.62 ± 0.04 spines/μm in WT [*n* = 10 cells]
171 and mGFAP Smo CKO [*n* = 10 cells], respectively, *p* = 0.71, 3 animals per genotype; **Figure 2 –**
172 **figure supplement 3**). This is in contrast to embryonic deletion of Shh from neurons using the
173 Emx-Cre driver, which produces a reduction in spine density of basal dendrites on layer V
174 neurons[16]. These data suggest that while the early stages of synapse formation proceed
175 independently of astrocytic Shh signaling, the maturing cortical circuit requires intact Shh activity
176 in astrocytes for the developmental pruning of excess synapses necessary to achieve its mature
177 organization.
178 To confirm that elevated spine density was due specifically to a loss of astrocytic Shh
179 signaling, we interrogated the spine density of pyramidal cells in two different regions where
180 Gli1 astrocytes are relatively sparse (see **Figure 1**). Pyramidal neurons in layer II/III of WT mice
181 showed a higher spine density than layer V neurons (0.79 ± 0.06 spines/μm, *n* = 7 cells, 4
182 animals) consistent with previous studies[27]. However, this was not significantly different from
183 the spine density observed in mGFAP Smo CKO mice (0.76 ± 0.06 spines/μm, *p* = 0.76, *n* = 9
184 cells, 5 animals; **Figure 2**). We also analyzed pyramidal neurons in the hippocampus.
185 Although the dentate gyrus of the hippocampus harbors a population of Gli1-expressing adult
186 neural progenitor cells, mature, differentiated astrocytes expressing Gli1 are relatively
187 sparse[14,28] (**Figure 1**). The spine density of CA1 pyramidal neurons in adult mice was higher
188 than in cortical neurons, consistent with previous studies[29,30]. However, there was no significant
189 difference in spine density between mGFAP Smo CKO mice and WT controls (0.97 ± 0.05
190 spines/μm and 0.90 ± 0.05 spines/μm in WT [*n* = 11 cells] and mGFAP Smo CKO [*n* = 11 cells],
191 respectively, *p* = 0.32, 3 animals per genotype; **Figure 2**). Our analysis of the recombination
192 pattern of the mGFAP-Cre driver showed that some cortical neurons undergo recombination
193 (**Figure 2 – figure supplement 1**). To rule out the possibility that Smo deletion in a small
194 population of neurons is responsible for the elevated spine density of layer V neurons, we
195 deleted Smo in excitatory neurons using the CamKIIα-Cre driver (CK2 Smo CKO), and
196 evaluated spine density of layer V neurons in adult mice. We found no significant difference in
197 spine density between CK2 Smo CKO mice and littermate controls (0.77 ± 0.07 spines/μm and
198 0.59 ± 0.06 spines/μm in WT [*n* = 10 cells] and CK2 Smo CKO [*n* = 9 cells], respectively, *p* =
199 0.07, 3 animals per genotype; **Figure 2**). Taken together, these data suggest that Shh activity
200 in astrocytes is necessary for the developmental reorganization of dendritic spines specifically
201 on layer V cortical neurons. Notably, we observed elevated spine density along the apical
202 dendrites of layer V neurons, which traverse layer II/III, where few Gli1 astrocytes are found.

203 This suggests that the modification of synapse organization mediated by Gli1 astrocytes does
204 not occur through direct astrocyte-synapse interactions.

205 Synapses are more stable in mGFAP Smo CKO mice

206 Dendritic spines are dynamic structures that undergo rapid formation and elimination during
207 postnatal cortical development. As cortical circuits mature, the fraction of spines undergoing
208 dynamic turnover declines concomitant with an increase in spine stability[26,27]. The dynamic
209 turnover of spines has long been considered a structural correlate of synaptic plasticity and can
210 be regulated in an activity-dependent manner[31–34]. To evaluate the role of astrocytic Shh
211 signaling in mediating spine dynamics, we performed repeated *in vivo* imaging of the apical tufts
212 of layer V neurons in the somatosensory cortex through a cranial window[35]. We confirmed the
213 layer V identity of imaged neurons by following individual dendritic segments to their soma and
214 created 3D reconstructions of imaged neurons. Only dendrites with soma in layer V, typically
215 500 μm – 600 μm from the surface of the brain, were analyzed. In Thy1-GFPm mice,
216 expression of GFP is developmentally regulated such that at P14, the intensity of GFP
217 expression and the density of fluorescently labeled neurons within the 3 mm cranial window is
218 insufficient for reliable imaging, as has been previously reported[27]. However by P17, GFP
219 expression was sufficiently dense and bright to enable reliable imaging. We analyzed the
220 fraction of spines undergoing dynamic turnover over 2 days in young mice at P17-P21 and P28-
221 P32. In WT mice, the turnover ratio was 0.14 at P17-P21 (n = 5 mice) and 0.10 in P28-P32
222 mice (n = 3 mice; **Figure 3**). In mGFAP Smo CKO mice however, the turnover ratio was lower
223 at P17-P21 than in WT mice, and remained stable at P28-P32 (0.11 and 0.10, respectively, n =
224 4 mice; **Figure 3**). This suggests that dendritic spines in mGFAP Smo CKO mice stabilize
225 earlier than those in WT mice. Consistent with this, we found that the fraction of filopodia was
226 lower in juvenile mGFAP Smo CKO mice compared to WT controls (**Figure 3**). Filopodia are
227 structural precursors of dendritic spines and exhibit higher rates of dynamic turnover than
228 mature spines[36,37]. Accordingly, the density of filopodia declines as the cortex matures[26,38].
229 Indeed, the fraction of all protrusions in juvenile WT mice (n = 7 mice) identified as filopodia was
230 25%, but that fraction declined significantly to 15% in adults (n = 16 mice, p = 0.0039; **Figure 3**).
231 In contrast, we did not observe this age-dependent decline in mGFAP Smo CKO mice (17% and
232 12% in juvenile [n = 10 mice] and adult [n = 7 mice] mGFAP Smo CKO mice, respectively, p =
233 0.398). The filopodial fraction in juvenile mGFAP Smo CKO mice was already significantly
234 below WT levels and comparable to adult WT levels, suggesting that nascent spines undergo
235 accelerated stabilization in the absence of astrocyte-mediated Shh signaling.

236 We performed further analysis of spine morphologies and classified spines as mature or
237 intermediate, to determine if there is an increase in mature spines. Protrusions with a
238 mushroom-like morphology were classified as mature, and thin protrusions lacking a discernible
239 spine head, or exhibiting a relatively dim, small head were identified as intermediate spines
240 (**Figure 3 – figure supplement 1**). In P17-21 mice, WT and CKO mice showed similar
241 proportions of mature spines (54% and 55% in WT and CKO, respectively, *n* = 4 mice per
242 genotype; **Figure 3**), however mGFAP Smo CKO mice showed an apparent increase in
243 protrusions with an intermediate morphology (16% and 26% in WT and CKO, respectively;
244 **Figure 3**), though this was not statistically significant. This suggests that these intermediate
245 protrusions reflect transitional morphologies as spines undergo maturation, and become more
246 stable. Consistent with this, adult mGFAP Smo CKO mice trended toward a modest increase in
247 the fraction of mature spines, compared to their WT controls (55% and 65% in WT and CKO,
248 respectively, *n* = 4 mice per genotype; **Figure 3 – figure supplement 1**), whereas the fraction
249 of intermediate spines was comparable at this age (27% and 23% in WT and CKO,
250 respectively).
251 It is well established that the rate of synaptic turnover declines considerably as animals
252 mature, reflecting an increase in stability of synaptic connections[26,27]. We next sought to
253 investigate the long-term stability of individual spines in adult mice by imaging dendrites weekly
254 for up to 6 weeks. We investigated the fraction of spines identified on the first day of imaging
255 that persisted in subsequent imaging sessions using custom written MATLAB code (**Figure 3 –**
256 **figure supplement 2**). We calculated the survival fraction by fitting to an exponential decay
257 model. This analysis revealed a larger proportion of long-lived stable spines in mGFAP Smo
258 CKO mice compared to WT control (71% and 79% in WT [*n* = 7 mice] and mGFAP Smo CKO [*n*
259 = 5 mice], respectively, $p = 0.0068$, Extra sum-of-squares F test; **Figure 3**), suggesting an
260 increase in stability of dendritic spines. Interestingly, among the population of dynamic spines,
261 we found two distinct populations consisting of transient spines, which disappeared and did not
262 reappear for the duration of the study, and recurrent spines, which disappeared and then
263 subsequently reappeared. Our data showed that the shift towards increased spine stability in
264 the mGFAP Smo CKO neurons was entirely due to a reduction in the proportion of recurrent
265 spines, with nearly identical fractions of transient spines observed across both genotypes
266 (**Figure 3**). These data suggest that structural plasticity is impaired in mGFAP Smo CKO mice.
267 This deficit in structural plasticity emerges during the third week of postnatal development and
268 persists into adulthood. Taken together, these data demonstrate that astrocyte-mediated Shh

signaling is required for establishing and maintaining the organization of cell type specific cortical synapses.

Shh signaling regulates Kir4.1 expression in cortical astrocytes

In both the developing and adult CNS, astrocytes directly eliminate synapses in an activity-dependent manner through MEGF10 and MERTK, two phagocytic receptors enriched in astrocytes[39]. To investigate whether these genes are negatively regulated in mGFAP Smo CKO mice, we examined their expression in the cortex of adult mice by quantitative PCR (qPCR). Expression of both *Mertk* and *Megf10* was comparable between WT and mGFAP Smo CKO mice (dCq values, *Mertk*: 5.97 ± 0.23 and 5.87 ± 0.06 in WT [n = 3 mice] and mGFAP Smo CKO [n = 6 mice], respectively, p = 0.54; *Megf10:* 8.02 ± 0.38 and 7.69 ± 0.18 in WT [n = 3 mice] and mGFAP Smo CKO [n = 6 mice], respectively, p = 0.39; **Figure 4 – figure supplement 1**). These data suggest that direct engulfment of synapses by astrocytes through these pathways is not regulated by Shh signaling and is not responsible for the increased spine density seen in mGFAP Smo CKO animals.

In the mature cerebellum, Shh signaling between Purkinje neurons and Bergmann glia regulates expression of the glial specific, inward-rectifying K^+ channel, Kir4.1[21]. In the cortex, the distribution of Kir4.1 exhibits a laminar pattern similar to that of Gli1 astrocytes, such that expression is enriched in layers IV and Vb, and reduced in layer Va (**Figure 4**). High resolution, confocal analysis showed that Kir4.1 is localized in the processes of Gli1 astrocytes (**Figure 4**). Kir4.1 expression is localized to astrocytic endfeet and is found surrounding neuronal somata in the spinal cord and brain[40–42]. In WT mice, expression of Kir4.1 surrounded many NeuN-positive neuronal somata in layer V (**Figure 4**). In mGFAP Smo CKO mice, however, there was a pronounced reduction in the expression of Kir4.1 throughout the cortex, and peri-somal Kir4.1 expression was severely diminished (**Figure 4**). In order to quantify expression levels of Kir4.1, we measured transcript abundance in the cortex of mGFAP Smo CKO mice and WT controls by droplet digital PCR (ddPCR). In mGFAP Smo CKO mice, there was a 50% reduction in *Kir4.1* transcripts compared to WT controls ($1.99 \times 10^6 \pm 1.93 \times 10^5$ copies/µl and $9.92 \times 10^5 \pm 8.49 \times 10^4$ copies/µl in WT [n = 6 mice] and mGFAP Smo CKO [n = 4 mice], respectively, p = 0.02). There was no difference in *Kir4.1* expression in CK2 Smo CKO mice compared to WT ($1.88 \times 10^6 \pm 3.77 \times 10^5$ copies/µl, p = 0.95, n = 4 mice; **Figure 4**), suggesting that downregulation of *Kir4.1* is due to astrocyte-specific, and not neuronal, disruption of Shh signaling. Conversely, GLAST-CreER-mediated deletion of the Shh receptor *Ptch1*, a negative regulator of Shh

301 signaling, dramatically upregulated Kir4.1 expression in the cortex (GLAST Ptch CKO; **Figure**
302 **4**). Kir4.1 expression is associated with glutamate uptake both *in vitro* and *in vivo*[43–45]. We
303 therefore measured expression levels of the astrocyte-specific glutamate transporters *GLAST*
304 and *GLT1*. There was no difference in expression of these genes in mGFAP Smo CKO mice
305 compared to WT (*GLT1*: $1.08 \times 10^7 \pm 6.6 \times 10^5$ copies/µl and $9.58 \times 10^6 \pm 2.1 \times 10^5$ copies/µl in
306 WT and mGFAP Smo CKO, respectively, $p = 0.15$, $n = 3$ mice per genotype; *GLAST*: 7.4×10^6
307 $\pm 4.4 \times 10^5$ copies/µl and $6.7 \times 10^6 \pm 6.5 \times 10^5$ copies/µl in WT and mGFAP Smo CKO,
308 respectively, $p = 0.41$, $n = 3$ mice per genotype; **Figure 4 – figure supplement 1**). It should be
309 noted that Kir4.1 was not restricted to Gli1 astrocytes in layers IV and Vb. Nevertheless, single
310 transcript quantification of Kir4.1 transcripts in mGFAP Smo CKO show a pronounced reduction,
311 suggesting that Kir4.1 expression in cortical astrocytes is regulated, in part, by Shh signaling.

312 Neurons exhibit hyperexcitability in mGFAP Smo CKO mice

313 To examine whether neurons in mGFAP Smo CKO mice exhibit disruptions in physiological
314 activity, we performed whole-cell patch clamp recordings of layer V pyramidal neurons from
315 coronal brain slices at P21, and examined action potential firing and membrane properties.
316 Using current clamp, we recorded action potential spikes per injected current at multiple step
317 currents from -300 pA to +650 pA. Our results revealed a significant increase in spike numbers
318 with high current injections (>500 pA) and total overall spikes in mGFAP Smo CKO animals
319 compared to WT control (326 ± 54 and 574 ± 71 spikes in WT [$n = 11$ cells from 4 animals] and
320 mGFAP Smo CKO [$n = 7$ cells from 3 animals], respectively, $p = 0.01$; **Figure 5**). We also
321 measured other membrane properties, including input resistance, resting membrane potential
322 and tau, and found no significant difference between mGFAP Smo CKO and WT neurons
323 (**Figure 5 – figure supplement 1**). However, we observed a significant decrease in action
324 potential threshold (-30.6 ± 2.0 and -37.9 ± 2.0 mV in WT and mGFAP Smo CKO, respectively,
325 $p = 0.0441$), accompanied by an increase in action potential amplitude (59.6 ± 2.6 and 73.3 ±
326 3.0 pA in WT and mGFAP Smo CKO, respectively, $p = 0.0083$), and a trending decrease in
327 action potential ½ width (1.0 ± 0.92 and 0.76 ± 0.02 ms in WT and mGFAP Smo CKO,
328 respectively, $p = 0.05$) in mGFAP Smo CKO neurons, consistent with an increase in neuron
329 excitability (**Figure 5**). Together, these results suggest mGFAP Smo CKO neurons exhibit an
330 increase in neuronal excitability consistent with excess extracellular K^+.
331 To examine excitatory synaptic transmission, we recorded spontaneous and miniature
332 excitatory postsynaptic currents (sEPSCs and mEPSCs) in layer V pyramidal neurons. We

333 found an increase in both the frequency (0.74 ± 0.08 and 1.18 ± 0.19 Hz in WT [*n* = 16 cells]
334 and mGFAP Smo CKO [*n* = 16 cells], respectively, *p* = 0.042) and amplitude (8.54 ± 0.38 and
335 11.33 ± 0.91 pA in WT and mGFAP Smo CKO, respectively, *p* = 0.008) of sEPSCs in slices
336 from mGFAP Smo CKO mice compared to WT control slices (4 animals per genotype; **Figure**
337 **5**). Furthermore, we observed an increase in the frequency (0.40 ± 0.05 and 1.10 ± 0.23 Hz in
338 WT and mGFAP Smo CKO, respectively, *p* = 0.003) and amplitude (7.54 ± 0.57 and 10.34 ±
339 0.74 pA in WT and mGFAP Smo CKO, respectively, *p* = 0.005) in mEPSCs in the presence of
340 tetrodotoxin (TTX), indicating an increase in postsynaptic response of neurons in mGFAP Smo
341 CKO mice (*n* = 14 and 11 cells from WT and mGFAP Smo CKO, respectively, 4 animals per
342 genotype; **Figure 5**). These data suggest that loss of Shh activity in astrocytes produces
343 disturbances in both pre and postsynaptic activity. Moreover, these data suggest that
344 astrocytes modulate both neuronal excitability and excitatory synaptic transmission in a Shh-
345 dependent manner.

346 Selective disruption of Shh signaling in astrocytes produces mild reactive 347 gliosis

348 We previously demonstrated that cortical astrocytes in mGFAP Smo CKO mice upregulate
349 GFAP expression and exhibit cellular hypertrophy, two classic hallmarks of reactive
350 astrogliosis[17]. Astrocytes exhibiting these features were broadly distributed across cortical
351 layers (**Figure 6**), in contrast to the distribution of Gli1 astrocytes which are found predominantly
352 in layers IV and V. In addition to upregulation of GFAP, astrocytes in mGFAP Smo CKO mice
353 show dramatic changes in morphological structure. Sholl analysis revealed no difference in the
354 number of primary branches in mGFAP Smo CKO mice compared to WT controls (7.2 and 7.5
355 branches, WT [*n* = 9 cells] and mGFAP Smo CKO [*n* = 9 cells], respectively, 3 animals per
356 genotype). However, astrocytes from mGFAP Smo CKO animals did show an increase in the
357 number of higher order branches, the length of the longest tree (136.6 ± 17 and 212.1 ± 28 μm
358 for WT and mGFAP Smo CKO, respectively, *p* = 0.035), and the total length of all processes
359 (397 ± 66 and 674 ± 91 μm for WT and mGFAP Smo CKO, respectively, *p* = 0.025) compared
360 to WT controls (**Figure 6**). Consistent with this, there was a significant increase in the number
361 of branches intersecting concentric shells at various distances from the soma (**Figure 6**).
362 Notably, in CK2 Smo CKO mice, GFAP staining in the cortex was indistinguishable from WT
363 controls (**Figure 6 – figure supplement 1**), suggesting that astrocytes exhibit dramatic changes
364 in morphological structure following astrocytic, but not neuronal, disruption of Shh signaling.

365 Such changes in morphology are consistent with mild reactive gliosis, a complex cellular
366 response of astrocytes to disturbances in physiological homeostasis[46]. Notably, the distribution
367 of reactive astrocytes in mGFAP Smo CKO mice is broader than that defined by Gli1
368 expression, arguing against the idea that Shh signaling regulates the intrinsic state of
369 astrocytes. Rather, reactive gliosis may instead reflect a cellular response to the mild, but
370 persistent, aberrations in neuronal activity observed in mGFAP Smo CKO mice.
371

372 # DISCUSSION

373 The dynamic processes underlying organization of synapses during postnatal development are
374 essential for establishing functional neural circuits. In this study, we demonstrate that
375 astrocytes modulate refinement and reorganization of synaptic connectivity in the postnatal
376 cortex in a Shh-dependent manner. Our data show that Gli1 astrocytes are enriched in deep
377 cortical layers with a relative paucity in upper cortical layers. Selective disruption of Shh
378 signaling in astrocytes leads to an overabundance of spines on the apical dendrites of layer V,
379 but not layer II/III, cortical neurons. The overabundance of spines emerges during postnatal
380 development, continues into adulthood and is accompanied by a reduction in dynamic turnover.
381 mGFAP Smo CKO mice exhibit a pronounced reduction in Kir4.1 as well as an increase in
382 neuronal excitability. Finally, we show that cortical astrocytes exhibit dramatic changes in
383 morphology and GFAP expression, a phenotype consistent with mild reactive gliosis. Our data
384 identify an essential role for astrocyte modulation of neuronal activity during postnatal
385 development, facilitating activity-dependent reorganization of synaptic connectivity.
386 To accomplish selective disruption of Shh signaling in astrocytes, we used a Cre driver
387 in which expression is regulated by the full-length mouse GFAP gene[22]. Single cell analysis in
388 *mGFAP-Cre*;Ai14 mice showed that nearly all cortical astrocytes undergo Cre-mediated
389 recombination, while the fraction of recombined cortical neurons is less than 2%. Importantly,
390 we observed recombined neurons predominantly in superficial layers, consistent with early Cre
391 activity during late embryogenesis when layer II/III neurons are being generated. Notably,
392 despite a small population of Smo null neurons in layer II/III, changes in spine density are not
393 observed in these cells. In addition, a more complete deletion of Smo in excitatory neurons
394 using the CamKIIαCre driver fails to alter spine density in layer V neurons, arguing against non-
395 specific effects arising from the small population of recombined neurons in mGFAP Smo CKO
396 mice. Importantly, Gli1 expression is nearly completely lost in mGFAP Smo CKO mice, with no
397 loss in the number of total astrocytes[17], demonstrating effective disruption of Shh activity in

398 these mice. Because a small number of recombined oligodendrocytes were observed in
399 *mGFAPCre*;Ai14 mice, the possibility that these cells may contribute to some of the observed
400 phenotypes cannot be ruled out. However Gli1 expression is restricted predominantly to
401 astrocytes in the adult forebrain[17]. Thus, any contribution from other cell types must be
402 mediated by non-canonical, Gli-independent mechanisms.
403 In the postnatal cortex, Shh signaling from layer V neurons mediates synaptic
404 connectivity with their layer II/III presynaptic partners[16]. Here, we show that, in addition to
405 neuronal Shh signaling, Shh activity in astrocytes is required for the establishment and
406 maintenance of cortical circuits. This is supported by two key observations in our study. First,
407 we find that in mGFAP Smo CKO mice, apical dendrites of cortical neurons exhibit an increase
408 in spine density that emerges during postnatal development and persists into adulthood.
409 Importantly, genetic deletion of *Smo* in mature neurons instead of astrocytes failed to show any
410 differences in spine density, pointing to a specific role for Shh signaling in astrocyte regulation of
411 synaptic connectivity. Interestingly, deletion of Shh ligand using an EmxCre driver produces a
412 reduction in spine density of basal dendrites[16], whereas we found no difference in basal dendrite
413 spine density, suggesting that Shh acts in distinct, cell type-specific ways to regulate synaptic
414 connectivity of local cortical circuits. Indeed, whereas astrocytes express Gli1, neurons do not[17],
415 indicating differential transduction of Shh through canonical and non-canonical, Gli-independent
416 pathways, respectively, in different cell types. Second, our data show fewer filopodia in juvenile
417 mGFAP Smo CKO mice compared to WT controls along with a concomitant increase in spine
418 stability. In the adult, spines continue to show deficits in dynamic turnover, demonstrating long-
419 term impairments in structural plasticity. This suggests that Shh signaling is required not only
420 for identifying appropriate synaptic partners during development, but also plays an important
421 role in mediating synaptic plasticity.
422 In the postnatal and adult brain, we and others identified neurons as the source of
423 Shh[16,17,21,47]. However non-neuronal sources, including astrocytes have been identified in the
424 injured brain[48,49]. Beyond the CNS, epithelial cells have been reported as a source of Shh in the
425 developing dentate gyrus[50]. It will be interesting to examine whether other non-neuronal
426 sources are available to trigger astrocyte transduction of Shh.
427 We previously demonstrated that Gli1 expression is restricted to a subpopulation of
428 cortical astrocytes[17]. Here, we extend these findings and demonstrate that the distribution of
429 Gli1 astrocytes in the cortex is not uniform across cortical layers, but rather, occurs in a laminar-
430 specific fashion. Cortical layers have been historically defined by neuronal populations and their
431 specific functional properties and connectivity. However, emerging evidence suggests that

432 astrocytes also exhibit cortical lamination patterns based on distinct gene expression
433 profiles[51,52]. Our data show that Gli1 astrocytes are enriched in layers IV and V with a relatively
434 sparse distribution in layer II/III. Interestingly, a recent study reported a population of astrocytes
435 with a similar distribution that show enrichment of the Shh pathway[52]. These cells were also
436 shown to regulate spine density of Layer V cortical neurons. It will be interesting to examine
437 whether these cells correspond to Gli1 astrocytes reported in this study. Whereas astrocytes
438 transducing Shh are enriched in deep cortical layers, the BMP antagonist, chordin-like 1
439 (Chrdl1) is preferentially enriched in upper layer cortical astrocytes[8], suggesting that Gli1 and
440 Chrdl1 may identify two distinct, but regionally complementary, astrocyte populations.
441 Alternatively, Shh signaling may actively repress Chrdl1 expression in deep layer astrocytes.
442 Notably, our observation that Gli1 astrocytes only comprise a fraction of astrocytes in layers IV
443 and V suggests that, in addition to the laminar-specific distribution of these cells, there may be
444 additional heterogeneity of astrocytes even within a given cortical layer. Whether and how the
445 laminar distribution of astrocytes with distinct gene expression profiles confers functional
446 specialization is not well understood and requires further study.
447 Interestingly, we observed that the disturbances in synaptic organization of cortical
448 neurons in mGFAP Smo CKO mice occurs selectively in apical dendrites of layer V, but not
449 layer II/III, neurons. Since apical dendrites of layer V neurons traverse through layer II/III, this
450 suggests that Shh-dependent regulation of synaptic refinement is not mediated by direct
451 interaction between Gli1 astrocytes and synapses. One possibility is that Gli1 astrocytes
452 interact with neuronal soma in layer V and effectively modulate their excitability. Our
453 observation that Kir4.1 expression in cortical astrocytes is regulated by Shh signaling suggests
454 that mGFAP Smo CKO mice may experience deficits in local buffering of extracellular K^+
455 leading to perturbations in neuronal activity. Indeed, a recent study demonstrated that Kir4.1
456 surrounds neuronal soma in the lateral habenula and regulates their firing properties[41].
457 Astrocytes play essential roles in buffering extracellular K^+ through Kir4.1, and several studies
458 demonstrate that loss of function of Kir4.1 impairs K^+ uptake and increases neuronal
459 excitability[44,45,53]. Alternatively, increased neuronal excitability may be due to disruptions in
460 glutamate clearance. Although we did not observe changes in expression of either GLT1 or
461 GLAST, deficits in Shh-dependent trafficking, localization or transporter function would lead to
462 impairments in astrocyte-mediated glutamate clearance. Further work is needed to definitively
463 identify the precise mechanism underlying the abnormal firing properties of neurons in mGFAP
464 Smo CKO mice.

465 The establishment of appropriate synapse number and connectivity are tightly regulated
466 processes that are profoundly shaped by experience or activity[34,54]. Our observation that
467 mGFAP Smo CKO mice show increases in spontaneous neuronal activity and excitability,
468 accompanied by a pronounced increase in spine density suggests that astrocytes contribute to
469 activity-dependent processes that shape the organization of developing neural circuits in a Shh-
470 dependent manner. The deficits in synaptic organization observed in mGFAP Smo CKO mice
471 persist for the life of the animal. These deficits are not limited to synapse number but also
472 include lower rates of spine turnover, suggesting long-lasting deficits in structural plasticity.
473 Together with the observation that Shh guides local synaptic connectivity of cortical neurons[16],
474 these studies reveal that Shh signaling exerts considerable influence on the establishment and
475 maintenance of cortical circuits.

476 METHODS

477 Key Resources Table

Reagent type (species) or resource	Designation	Source or reference	Identifiers	Additional information
Genetic reagent (M. musculus)	*Gli1*$^{CreER/+}$	The Jackson Laboratory; Ahn and Joyner, 2005, PMID: 16208373	stock no. 7913	from Alexandra Joyner, MSKCC
Genetic reagent (M. musculus)	Ai14 (B6.Cg-Gt(ROSA)26Sor$^{tm14(CAG-tdTomato)Hze}$/J)	The Jackson Laboratory; Madisen et al., 2010, PMID: 20023653	stock no. 7914	
Genetic reagent (M. musculus)	mGFAP-Cre, line 73.12	The Jackson Laboratory; Garcia et al., 2004, PMID: 15494728	stock no. 12886	from Michael Sofroniew, UCLA
Genetic reagent (M. musculus)	*Smo*$^{fl/fl}$	The Jackson Laboratory; Long et al., 2001, PMID: 11748145	stock no. 4526	

Genetic reagent (M. musculus)	CamKinaseIIα-Cre (CamKIIα-Cre)	The Jackson Laboratory; Tsien JZ et al., 1996, PMID: 8980237	stock no. 5359	
Genetic reagent (M. musculus)	Thy1-GFPm	The Jackson Laboratory; Feng G et al., 2000, PMID: 11086982	stock no. 7788	
chemical compound, drug	tamoxifen	Sigma	catalog no. T5648	
antibody	rb anti-GFP	Millipore	catalog no. AB3080	brightfield (1:5,000); fluorescence (1:1,000)
antibody	rb anti-Kir4.1	Millipore	catalog no. AB5818	(1:1,000)
antibody	rb anti-GFAP	Agilent DAKO	catalog no. Z033429-2;	(1:20,000)
antibody	ms anti-NeuN	Millipore	catalog no. MAB377	(1:1,000)
antibody	rb anti-RFP	MBL International	catalog no. PM005	(1:500)
antibody	rat anti-Ctip2	Abcam	catalog no. ab18465	(1:2,000)
antibody	sh anti-CAII	Bio-Rad	catalog no. AHP206	(1:2,000)
antibody	rb anti-S100B	Agilent	catalog no. Z0311	(1:1,000)
antibody	rabbit anti-Olig2	Millipore	catalog no. AB9610	(1:1,000)
software, algorithm	computer assisted tracing of dendrites and spines; Sholl analysis of astrocytes	Neurolucida, MBF Biociences		Williston, VT
software, algorithm	custom-written code for longituinal analysis of spine turnover	this paper		MATLAB-based

478

479 *Animals*

480 All experiments were approved by Drexel University's Institutional Animal Care and Use
481 Committee and were conducted according to approved protocols. We used the following strains
482 of transgenic mice on the C57BL/6 background: *Gli1*$^{CreER/+}$ [14], Ai14 [55], *Smo*$^{fl/fl}$ [56], *mGFAP-Cre*[22],
483 *CaMKIIa-Cre*[57] and *Thy1-GFPm*[25]. Mice of either sex were included in these studies.

484 *Tamoxifen*

485 Tamoxifen was administered as previously described[17,20]. Briefly, tamoxifen (Sigma, T5648)
486 was dissolved in corn oil to a final concentration of 20 mg/ml. Adult *Gli1*$^{CreER/+}$*;Ai14* mice
487 received 250mg/kg tamoxifen by oral gavage for three consecutive days, and tissues were
488 analyzed two – three weeks later.

489 *Immunohistochemistry*

490 Mice were deeply anesthetized by intraperitoneal injection of ketamine/xylazine/acepromazine.
491 Animals were then transcardially injected with 100 units heparin and perfused with phosphate-
492 buffered saline (PBS) followed by 4% paraformaldehyde (PFA, Sigma-Aldrich, St. Louis, MO).
493 Brains were fixed overnight at 4°C and then transferred to 30% sucrose for at least 48 hours or
494 until sectioned. Brains were cryosectioned (Leica CM3050S, Wetzlar, Germany) and collected
495 in 40 μm sections. Sections were stored in 0.1M Tris-buffered saline (TBS) with 0.05% sodium
496 azide at 4°C. Immunohistochemistry was performed using the following primary antibodies:
497 rabbit anti-GFP (AB3080; Millipore, Burlington, MA), rabbit anti-Kir4.1 (AB5818; Millipore), rabbit
498 anti-GFAP (Z033429-2; Agilent DAKO, Santa Clara, CA), mouse anti-NeuN (MAB377;
499 Millipore), rabbit anti-RFP (PM005; MBL International, Woburn, MA), rat anti-Ctip2 (ab18465;
500 Abcam, Cambridge, UK), sheep anti-CAII (AHP206; Bio-Rad), rabbit anti-S100β (Z0311,
501 Agilent), and rabbit anti-Olig2 (AB9610; Millipore). Sections were washed three times in 0.1M
502 TBS at room temperature (10 minutes/wash). Sections were then blocked in 10% Normal
503 Serum with 0.5% Triton-X (Sigma-Aldrich) for one hour at room temperature and incubated with
504 primary antibody in 0.5% Triton-X at 4°C overnight. For fluorescent immunohistochemistry,
505 sections were rinsed the following day in 0.1M TBS and incubated in Alexafluor-conjugated
506 secondary antibodies with 10% Normal Serum and 0.1M TBS and incubated at room
507 temperature for two hours. The sections were then rinsed in 0.1 TBS and incubated in DAPI
508 (1:50,000; Life Technologies, Carlsbad, CA) for 15 minutes. Sections were rinsed again in 0.1M
509 TBS and mounted onto microscope slides (Fisherbrand, Waltham, MA) and coverslipped using
510 ProLong Gold Antifade Mountant (Invitrogen, Carlsbad, CA) and Fisherfinest Premium Cover

511 Glass. For brightfield immunohistochemistry, sections were rinsed as previously described but
512 were incubated with biotinylated secondary antibodies against the primary antibody species
513 (Vector Laboratories, Burlingame, CA) for one hour. Sections were then placed in Avitin-Biotin
514 Complex solution (Vector) for one hour and visualized using 3,3'-diaminobenzidine (DAB
515 Peroxidase Substrate Kit, Vector). Sections were then mounted onto slides and coverslipped
516 with DPX Mountant (Fisher).

517 *Quantification of dendritic spine density*

518 Analysis of spine density was performed in a blinded study design. WT controls were derived
519 from Cre-negative littermates. Neurons were traced using Neurolucida (MicroBrightField
520 Biosciences, Williston, VT) and individual spines were marked. Apical dendrites of layer V
521 neurons were counted from ~100 μm below the primary bifurcation through the apical tuft.
522 Apical dendrites of layer II/III cells were analyzed just below the primary bifurcation through the
523 apical tuft. Basal dendrites were analyzed beginning ~50 μm from the soma through the end of
524 the processes. CA1 hippocampal neurons were analyzed from just below the primary bifurcation
525 through the apical tuft. All analysis was performed on an upright Zeiss microscope using a 63X
526 oil objective.

527 *Cranial window*

528 Cranial window surgeries were adapted from a published protocol[35]. Immediately prior to each
529 surgery, mice received a subcutaneous injection of carprofen (Rimadyl, 5 mg/kg), and a follow-
530 up injection was given 24 hours after surgery. Mice were deeply anesthetized with isoflurane
531 (5%) in an induction chamber, and then transferred to a stereotaxic apparatus where they
532 inhaled 1.5% isoflurane continuously for the duration of the surgery. The scalp was then
533 removed and a metal bar (~1 cm long) with threadings for screws was affixed to the skull, using
534 superglue and dental acrylic to form a head post that sealed off the skin while leaving the right
535 parietal bone exposed. After allowing 24 hours for the glue and acrylic to set, the mouse was
536 returned to the stereotaxic apparatus and head-fixed using the headpost. A circular craniotomy
537 ~3 mm in diameter and centered 2.5 mm lateral and posterior to bregma was performed. The
538 exposed dura was treated with saline-soaked gel foam until any minor bleeding ceased. Finally,
539 a 3 mm glass coverslip was gently pressed onto the dura and sealed in place using superglue
540 and dental acrylic. Adult mice were allowed at least 1 week for recovery. To mitigate the
541 tendency of rapid bone growth to destabilize the windows at younger ages, juvenile mice were
542 allowed 24 hours to recover.

543 *Two-photon imaging*

544 A commercial two-photon microscope (Bruker, Billerica, MA) with a tunable Ti:Sapphire laser
545 (Coherent, Santa Clara, CA) was used for all experiments. The laser was set to 920 nm and
546 power was tuned on the sample as necessary to obtain consistently high-quality images without
547 damaging the tissue. Mice were head-fixed and anesthetized with continuous isoflurane (1-
548 1.5%) during imaging. Under a 20X water immersion objective, GFP-expressing neurons were
549 identified visually and then imaged down to the cell body to determine layer. From the apical
550 dendrite tuft, individual dendrite segments that projected primarily along the xy-plane were
551 selected for analysis, and z-stacks (0.5 μm step size) were collected. To track individual
552 dendrites, repeated imaging was generally performed on the following schedule (in days,
553 relative to first imaging session): 0, 1, 2, 7, 14, 21, 28, 42. Some data from studies using other
554 schedules were also included. For juvenile mice, this schedule was: 0, 1, 2.

555 *Analysis of spine dynamics*

556 Every effort was made to use Cre-negative, littermate controls for these experiments. However,
557 it was not always possible to match littermate controls in the final data sets presented here,
558 either due to the absence of the GFP allele in the Cre-negative controls, or due to the loss of
559 head caps securing the cranial windows, over time. However, it should be noted that all data
560 presented here represent Cre-negative controls from the appropriate strain, if not necessarily
561 from the same litter.

562 To analyze spine turnover, we performed side-by-side manual comparison of dendritic
563 protrusions using ImageJ. Z-stacks from two time points were analyzed, and individual
564 protrusions were identified as present or absent in each stack. For each mouse, a minimum of
565 150 protrusions were analyzed, although the average number of protrusions analyzed per
566 mouse was 250-300. These comparisons were conducted by trained observers blinded to
567 mouse genotype. Long, thin protrusions lacking a bulbous head were identified as filopodia, and
568 any other prominent dendritic protrusion that extended > 0.4 μm from the shaft was counted as
569 a spine. The filopodial fraction was calculated as the proportion of all analyzed features present
570 at the first imaging timepoint that were identified as filopodia. The position and dynamic status
571 (stable/eliminated/formed) of each spine was recorded using ImageJ's CellCounter plugin. Each
572 neuron's turnover ratio was calculated as:

573 $$TO = (N_{elim} + N_{form})/(N_{elim} + N_{form} + 2N_{stable})$$

574 For longitudinal analysis of spine lifetime, the individual features identified in our manual
575 ImageJ analysis were then imported into custom written MATLAB (Mathworks, Natick, MA)
576 code and manually tracked across all imaged time-points using custom-written software. This
577 code facilitated the efficient manual tracking of each feature by iteratively estimating the z-
578 plane, within each stack, in which that feature would be expected to appear, assuming a linear
579 relationship. Using a graphical user interface, the user was presented with a series of frames
580 centered on that plane and allowed to make a determination of the feature's presence or
581 absence simply by left-clicking on the feature, or in the case of absence right-clicking on the
582 location it otherwise would have been, using the best frame presented (**Figure 3 – figure**
583 **supplement 2**). Due to the iterative nature of this procedure, each dataset was run through at
584 least twice to ensure that not only were the determinations of presence/absence accurate, but
585 that the marked locations of every feature were optimal.

586 Spines that were observed consistently across all time points were classified as stable. Spines
587 that disappeared at some time point and were observed again in a subsequent time point were
588 classified as recurrent. Spines that disappeared and never reappeared were classified as
589 transient. To compare long-term dynamics between WT and mGFAP Smo CKO mice, we
590 examined the survival curves, S(t), for each mouse, where:

591 S(t) = # of spines consistently present to time point t / # of spines initially observed

592 Survival curves for each mouse were pooled by genotype and fit to a single-phase exponential
593 decay model:

594 $$S(t) = S_p + S_i * \exp(-t/\tau)$$

595 where S_p and S_i represent the relative fractions of permanent and impermanent spines
596 respectively and τ is the characteristic lifespan of impermanent spines. Fitting and statistical
597 comparison of survival data was performed with PRISM 6 (GraphPad, San Diego, CA) software.

598 To analyze morphology, we examined data from the first imaged day, and classified individual
599 protrusions as filopodia, intermediate, or mushroom spines. For each protrusion, a mean
600 projection image was generated, averaging the frame on which the protrusion was manually
601 marked in the original analysis and the 2 neighboring frames (1 above and 1 below, effectively
602 averaging over 1.5 um of depth in the z axis). Each image was cropped, centering around the
603 protrusion's XY coordinates and a marker was drawn on the image to indicate which protrusion
604 was under consideration. These images were then presented to the scorer sequentially for
605 scoring. Protrusions exhibiting a bright, bulbous head were scored as mushroom. Thin

606 protrusions exhibiting a relatively dim, small head, or no head, were scored as intermediate.
607 Dim, elongated protrusions that lacked any head were scored as filopodia.

608 *Transcript Quantification*

609 Mice were deeply anesthetized by intraperitoneal injection of ketamine/xylazine/acepromezine
610 before rapid decapitation. Cortices were dissected into TRIzol reagent (Thermo-Fisher,
611 Waltham, MA) and RNA was extracted according to the standard protocol. RNA was then
612 purified with an RNeasy Micro Kit (Qiagen, Hilden, Germany) and subsequently reverse
613 transcribed to cDNA using the High-Capacity cDNA Reverse Transcription Kit (Thermo-Fisher).
614 Droplet digital PCR (ddPCR) was performed with the QX200 Droplet Digital PCR System using
615 Evagreen Supermix (Bio-Rad, Hercules, CA). Alternatively, for *Megf10* and *Mertk*, qPCR was
616 performed with the CFX96 Touch Real-Time PCR Detection System (Bio-Rad) using PowerUp
617 SYBR Green Master Mix (Thermo-Fisher). PrimePCR ddPCR Expression EvaGreen Assay
618 (Bio-Rad) was used for *Gapdh* primers; all other primers were designed using NCBI Primer-
619 BLAST as follows: *Kir4.1* F, GCTGCCCCGCGATTTATCAG; *Kir4.1* R,
620 AGCGACCGACGTCATCTTGG; *GLAST* F, TCCTCTACTTCCTGGTAACCC; *GLAST* R,
621 TCCACACCATTGTTCTCTTCC; *Glt1* F, CATCAACAGAGGGTGCCAAC; *Glt1* R,
622 CACACTGCTCCCAGGATGAC; *Megf10* F, CTCACTGCTCTGTCACTGGGTG; *Megf10* R,
623 GGTAGCTGATTCTGTGCCGTGT; *Mertk* F, AAACTGCATGTTGCGGGATGAC; *Mertk* R,
624 TCCCACATGGTCACGCCAAA. ddPCR absolute quantification of targets was calculated using
625 Quantasoft Version 1.7 software (Bio-Rad). Samples were run in triplicate, and *Gapdh* was
626 quantified for each sample as a loading control with no difference detected between sample
627 groups.

628 *Slice electrophysiology*

629 Mice aged P21 were anesthetized with intraperitoneal injection of euthasol (0.2 ml/kg) and
630 brains were rapidly removed. 300 µm coronal slices were cut using a vibratome tissue slicer
631 (Leica) and transferred to a holding chamber, submerged in oxygenated artificial cerebrospinal
632 fluid (ACSF, in mM: 124 NaCl, 2.5 KCl, 1.25 NaH_2PO_4, 2 $CaCl_2$, 1 $MgSO_4$, 26 $NaHCO_3$, and 10
633 dextrose, pH 7.4) at 36°C for 1 hour and then maintained at room temperature. Individual slices
634 containing the barrel cortex were placed into a recording chamber immersed in oxygenated
635 ACSF mounted on an Olympus upright microscope (BX51). Neurons were visualized with
636 infrared differential interference video microscopy.

637 Whole-cell current clamp was used to record action potentials from layer V pyramidal cells using
638 patch electrodes with an open tip resistance of 7–10 MΩ. Patch electrodes were filled with
639 potassium gluconate internal solution (in mM): 120 potassium gluconate, 20 KCl, 4 ATP-Na, 0.3
640 Na_2GTP, 5 Na-phosphocreatine, 0.1 EGTA, 10 HEPES, pH 7.3, 305 mosmol/l) and action
641 potential responses were measured in response to various step currents from -300 pA to +650
642 pA with 50 pA increments. Action potentials were described as spike numbers per depolarized
643 current injections. The resting membrane potential, input resistance, action potential (AP)
644 threshold, AP half-width, and peak AP amplitude were also measured.

645 Whole-cell voltage-clamp recordings were obtained from layer V pyramidal cells using patch
646 electrodes with Cs^+-containing solution (in mM): 120 Cs-gluconate, 5 lidocaine, 6 $CaCl_2$, 1
647 Na_2ATP, 0.3 Na_2GTP, and 10 HEPES (pH 7.3 adjusted by CsOH). To record spontaneous
648 excitatory postsynaptic currents (sEPSCs), cells were held at a membrane potential of -70mV in
649 the presence of $GABA_A$ receptor antagonist picrotoxin (PTX; 100 μM, Sigma-Aldrich) and
650 recorded for 5 minutes. Miniature EPSCs (mEPSCs) were then recorded for an additional 5
651 minutes in the presence of both picrotoxin and tetrodotoxin (TTX, 0.5 μM, Hello Bio, Princeton,
652 NJ). All recordings were conducted with Axon MultiClamp 700B amplifier (Molecular Devices,
653 San Jose, CA). The sEPSCs and mEPSCs frequency and amplitudes were measured by
654 averaging 5 sweeps from the onset of recording with Clampfit 9.2 software (Molecular Devices).
655 The s/mEPSCs were detected and characterized using a sample template for the 5-minute data
656 period. Based upon the selected sample template, the frequency (number of event detections)
657 and amplitude of events were measured using a threshold set in Clampfit.

658 *Statistical Analyses*

659 Statistical analyses used for various datasets are indicated both in the figure legends and in the
660 text. Prism 6 software (GraphPad) was used for all analyses and to generate graphs.

661 Acknowledgements

662 We would like to thank Pooja Sakthivel and Nikhil Karmacharya for technical assistance and Dr.
663 Monica Truelove-Hill for assistance with statistical analyses. We also thank Dr. Michael Akins
664 for helpful discussions.

665

REFERENCES

1. Penzes, P., Cahill, M. E., Jones, K. A., Vanleeuwen, J. E. & Woolfrey, K. M. Dendritic spine pathology in neuropsychiatric disorders. *Nat. Neurosci.* **14**, 285–293 (2011). DOI: 10.1038/nn.2741

2. Allen, N. J. & Eroglu, C. Cell Biology of Astrocyte-Synapse Interactions. *Neuron* **96**, 697–708 (2017). DOI: 10.1016/j.neuron.2017.09.056

3. Adamsky, A., Kol, A., Groysman, M., London, M., Kreisel, T., Doron, A., Ozeri-Engelhard, N., Melcer, T., Refaeli, R., Horn, H., Regev, L. & Goshen, I. Astrocytic Activation Generates De Novo Neuronal Potentiation and Memory Enhancement. *Cell* **174**, 59–71 (2018). DOI: 10.1016/j.cell.2018.05.002

4. Risher, W. C., Patel, S., Kim, I. H. wan, Uezu, A., Bhagat, S., Wilton, D. K., Pilaz, L. J., Singh Alvarado, J., Calhan, O. Y., Silver, D. L., Stevens, B., Calakos, N., Soderling, S. H. & Eroglu, C. Astrocytes refine cortical connectivity at dendritic spines. *Elife* **3**, 166–175 (2014). DOI: 10.7554/eLife.04047

5. Allen, N. J., Bennett, M. L., Foo, L. C., Wang, G. X., Chakraborty, C., Smith, S. J. & Barres, B. A. Astrocyte glypicans 4 and 6 promote formation of excitatory synapses via GluA1 AMPA receptors. *Nature* **486**, 410–4 (2012). DOI: 10.1038/nature11059

6. Kucukdereli, H., Allen, N. J., Lee, A. T., Feng, A., Ozlu, M. I., Conatser, L. M., Chakraborty, C., Workman, G., Weaver, M., Sage, E. H., Barres, B. A. & Eroglu, C. Control of excitatory CNS synaptogenesis by astrocyte-secreted proteins Hevin and SPARC. *Proc. Natl. Acad. Sci. U. S. A.* **108**, E440-9 (2011). DOI: 10.1073/pnas.1104977108

7. Christopherson, K. S., Ullian, E. M., Stokes, C., Mullowney, C., Hell, J., Agah, A., Lawler, J., Mosher, D., Bornstein, P. & Barres, B. A. Thrombospondins are astrocyte-secreted proteins that promote CNS synaptogenesis. *Cell* **120**, 421–433 (2005).

8. Blanco-Suarez, E., Liu, T.-F., Kopelevich, A. & Allen, N. J. Astrocyte-Secreted Chordin-like 1 Drives Synapse Maturation and Limits Plasticity by Increasing Synaptic GluA2 AMPA Receptors. *Neuron* 1–17 (2018). DOI: 10.1016/j.neuron.2018.09.043

9. Chung, W. S., Allen, N. J. & Eroglu, C. Astrocytes control synapse formation, function, and elimination. *Cold Spring Harb. Perspect. Biol.* **7**, a020370 (2015). DOI: 10.1101/cshperspect.a020370

10. Olsen, M. L. & Sontheimer, H. Functional implications for Kir4.1 channels in glial biology: From K + buffering to cell differentiation. *Journal of Neurochemistry* **107**, 589–601 (2008). DOI: 10.1111/j.1471-4159.2008.05615.x

11. Fuccillo, M., Joyner, A. L. & Fishell, G. Morphogen to mitogen: the multiple roles of hedgehog signalling in vertebrate neural development. *Nat. Rev. Neurosci.* **7**, 772–83 (2006). DOI: 10.1038/nrn1990

12. Ruiz i Altaba, A., Palma, V. & Dahmane, N. Hedgehog–Gli Signalling and the Growth of the Brain. *Nat. Rev. Neurosci.* **3**, 24–33 (2002). DOI: 10.1038/nrn704

13. Traiffort, E., Angot, E. & Ruat, M. Sonic Hedgehog signaling in the mammalian brain. *Journal of Neurochemistry* **113**, 576–590 (2010). DOI: 10.1111/j.1471-4159.2010.06642.x

14. Ahn, S. & Joyner, A. L. In vivo analysis of quiescent adult neural stem cells responding to Sonic hedgehog. *Nature* **437**, 894–897 (2005). DOI: 10.1038/nature03994

15. Ihrie, R. A., Shah, J. K., Harwell, C. C., Levine, J. H., Guinto, C. D., Lezameta, M., Kriegstein, A. R. & Alvarez-Buylla, A. Persistent Sonic Hedgehog Signaling in Adult Brain Determines Neural Stem Cell Positional Identity. *Neuron* **71**, 250–262 (2011). DOI: 10.1016/j.neuron.2011.05.018

16. Harwell, C. C., Parker, P. R. L., Gee, S. M., Okada, A., McConnell, S. K., Kreitzer, A. C. & Kriegstein, A. R. Sonic Hedgehog Expression in Corticofugal Projection Neurons Directs Cortical Microcircuit Formation. *Neuron* **73**, 1116–1126 (2012). DOI: 10.1016/j.neuron.2012.02.009

17. Garcia, A. D. R., Petrova, R., Eng, L. & Joyner, A. L. Sonic hedgehog regulates discrete populations of astrocytes in the adult mouse forebrain. *J. Neurosci.* **30**, 13597–608 (2010). DOI: 10.1523/JNEUROSCI.0830-10.2010

18. Garcia, A. D. R., Han, Y.-G., Triplett, J. W., Farmer, W. T., Harwell, C. C. & Ihrie, R. A. The Elegance of Sonic Hedgehog: Emerging Novel Functions for a Classic Morphogen. *J. Neurosci.* **38**, 9338–9345 (2018). DOI: 10.1523/JNEUROSCI.1662-18.2018

19. Alvarez, J. I., Dodelet-Devillers, A., Kebir, H., Ifergan, I., Fabre, P. J., Terouz, S., Sabbagh, M., Wosik, K., Bourbonnière, L., Bernard, M., Van Horssen, J., De Vries, H. E., Charron, F. & Prat, A. The hedgehog pathway promotes blood-brain barrier integrity and CNS immune quiescence. *Science (80-.).* **334**, 1727–1731 (2011). DOI: 10.1126/science.1206936

20. Allahyari, R. V., Clark, K. L., Shepard, K. A. & Garcia, A. D. R. Sonic hedgehog signaling is negatively regulated in reactive astrocytes after forebrain stab injury. *Sci. Rep.* **9**, 565 (2019). DOI: 10.1038/s41598-018-37555-x

21. Farmer, W. T., Abrahamsson, T., Chierzi, S., Lui, C., Zaelzer, C., Jones, E. V, Bally, B. P., Chen, G. G., Théroux, J.-F., Peng, J., Bourque, C. W., Charron, F., Ernst, C., Sjöström, P. J. & Murai, K. K. Neurons diversify astrocytes in the adult brain through sonic hedgehog signaling. *Science (80-.).* **351**, 849–854 (2016). DOI: 10.1126/science.aab3103

22. Garcia, A. D. R., Doan, N. B., Imura, T., Bush, T. G. & Sofroniew, M. V. GFAP-expressing progenitors are the principal source of constitutive neurogenesis in adult mouse forebrain. *Nat. Neurosci.* **7**, 1233–1241 (2004). DOI: 10.1038/nn1340

23. Vooijs, M., Jonkers, J. & Berns, A. A highly efficient ligand-regulated Cre recombinase mouse line shows that LoxP recombination is position dependent. *EMBO Rep.* **2**, 292–297 (2001). DOI: 10.1093/embo-reports/kve064

24. Nimchinsky, E. A., Sabatini, B. L. & Svoboda, K. Structure and Function of Dendritic Spines. *Annu. Rev. Physiol.* **64**, 313–353 (2002). DOI: 10.1146/annurev.physiol.64.081501.160008

25. Feng, G., Mellor, R. H., Bernstein, M., Keller-Peck, C., Nguyen, Q. T., Wallace, M., Nerbonne, J. M., Lichtman, J. W. & Sanes, J. R. Imaging Neuronal Subsets in Transgenic Mice Expressing Multiple Spectral Variants of GFP. *Neuron* **28**, 41–51 (2000). DOI: 10.1016/S0896-6273(00)00084-2

26. Zuo, Y., Lin, A., Chang, P. & Gan, W.-B. Development of Long-Term Dendritic Spine

751 Stability in Diverse Regions of Cerebral Cortex. *Neuron* **46**, 181–189 (2005). DOI:
752 10.1016/j.neuron.2005.04.001

753 27. Holtmaat, A., Trachtenberg, J. T., Wilbrecht, L., Shepherd, G. M., Zhang, X., Knott, G. W.
754 & Svoboda, K. Transient and persistent dendritic spines in the neocortex in vivo. *Neuron*
755 **45**, 279–291 (2005). DOI: 10.1016/j.neuron.2005.01.003

756 28. Han, Y. G., Spassky, N., Romaguera-Ros, M., Garcia-Verdugo, J. M., Aguilar, A.,
757 Schneider-Maunoury, S. & Alvarez-Buylla, A. Hedgehog signaling and primary cilia are
758 required for the formation of adult neural stem cells. *Nat. Neurosci.* **11**, 277–284 (2008).
759 DOI: 10.1038/nn2059

760 29. Attardo, A., Fitzgerald, J. E. & Schnitzer, M. J. Impermanence of dendritic spines in live
761 adult CA1 hippocampus. *Nature* **523**, 592–596 (2015). DOI: 10.1038/nature14467

762 30. Perez-Cruz, C., Nolte, M. W., Van Gaalen, M. M., Rustay, N. R., Termont, A., Tanghe, A.,
763 Kirchhoff, F. & Ebert, U. Reduced Spine Density in Specific Regions of CA1 Pyramidal
764 Neurons in Two Transgenic Mouse Models of Alzheimer's Disease. *J. Neurosci.* **31**,
765 3926–3934 (2011). DOI: 10.1523/JNEUROSCI.6142-10.2011

766 31. Lendvai, B., Stern, E. a, Chen, B. & Svoboda, K. Experience-dependent plasticity of
767 dendritic spines in the developing rat barrel cortex in vivo. *Nature* **404**, 876–881 (2000).
768 DOI: 10.1038/35009107

769 32. Trachtenberg, J. T., Chen, B. E., Knott, G. W., Feng, G., Sanes, J. R., Welker, E. &
770 Svoboda, K. Long-term in vivo imaging of experience-dependent synaptic plasticity in
771 adult cortex. *Nature* **420**, 788–794 (2002). DOI: 10.1038/nature01273

772 33. Holtmaat, A. & Svoboda, K. Experience-dependent structural synaptic plasticity in the
773 mammalian brain. *Nat. Rev. Neurosci.* **10**, 647–658 (2009). DOI: 10.1038/nrn2721

774 34. Zuo, Y., Yang, G., Kwon, E. & Gan, W.-B. Long-term sensory deprivation prevents
775 dendritic spine loss in primary somatosensory cortex. *Nature* **436**, 261–265 (2005). DOI:
776 10.1038/nature03715

777 35. Holtmaat, A., Bonhoeffer, T., Chow, D. K., Chuckowree, J., De Paola, V., B, H. S.,
778 Hübener, M., Keck, T., Knott, G., Lee, W.-C. A., Mostany, R., Mrsic-Flogel, T. D., Nedivi,
779 E., Portera-Cailliau, C., Svoboda, K., Trachtenberg, J. T. & Wilbrecht, L. Long-term, high-
780 resolution imaging in the mouse neocortex through a chronic cranial window. *Nat. Protoc.*
781 **4**, 1128–44 (2009). DOI: 10.1038/nprot.2009.89

782 36. Ziv, N. E. & Smith, S. J. Evidence for a role of dendritic filopodia in synaptogenesis and
783 spine formation. *Neuron* **17**, 91–102 (1996). DOI: 10.1016/S0896-6273(00)80283-4

784 37. Berry, K. P. & Nedivi, E. Spine Dynamics: Are They All the Same? *Neuron* **96**, 43–55
785 (2017). DOI: 10.1016/j.neuron.2017.08.008

786 38. Grutzendler, J., Kasthuri, N. & Gan, W. B. W.-B. Long-term dendritic spine stability in the
787 adult cortex. *Nature* **420**, 812–816 (2002). DOI: 10.1038/nature01151.1.

788 39. Chung, W.-S., Clarke, L. E., Wang, G. X., Stafford, B. K., Sher, A., Chakraborty, C.,
789 Joung, J., Foo, L. C., Thompson, A., Chen, C., Smith, S. J. & Barres, B. a. Astrocytes
790 mediate synapse elimination through MEGF10 and MERTK pathways. *Nature* **504**, 394–
791 400 (2013). DOI: 10.1038/nature12776

792 40. Kelley, K. W., Ben Haim, L., Schirmer, L., Tyzack, G. E., Tolman, M., Miller, J. G., Tsai,

793 H. H., Chang, S. M., Molofsky, A. V., Yang, Y., Patani, R., Lakatos, A., Ullian, E. M. &
794 Rowitch, D. H. Kir4.1-Dependent Astrocyte-Fast Motor Neuron Interactions Are Required
795 for Peak Strength. *Neuron* 1–14 (2018). DOI: 10.1016/j.neuron.2018.03.010

796 41. Cui, Y., Yang, Y., Ni, Z., Dong, Y., Cai, G., Foncelle, A., Ma, S., Sang, K., Tang, S., Li, Y.,
797 Shen, Y., Berry, H., Wu, S. & Hu, H. Astroglial Kir4.1 in the lateral habenula drives
798 neuronal bursts in depression. *Nature* **554**, 323–327 (2018). DOI: 10.1038/nature25752

799 42. Higashi, K., Fujita, A., Inanobe, A., Tanemoto, M., Doi, K., Kubo, T. & Kurachi, Y. An
800 inwardly rectifying K(+) channel, Kir4.1, expressed in astrocytes surrounds synapses and
801 blood vessels in brain. *Am J Physiol Cell Physiol* **281**, C922-31 (2001). DOI:
802 10.1002/cne.903280405

803 43. Kucheryavykh, Y. V., Kucheryavykh, L. Y., Nichols, C. G., Maldonado, H. M., Baksi, K.,
804 Reichenbach, A., Skatchkov, S. N. & Eaton, M. J. Downregulation of Kir4.1 inward
805 rectifying potassium channel subunits by RNAi impairs potassium transfer and glutamate
806 uptake by cultured cortical astrocytes. *Glia* **55**, 274–281 (2007). DOI: 10.1002/glia.20455

807 44. Djukic, B., Casper, K. B., Philpot, B. D., Chin, L. S. & McCarthy, K. D. Conditional knock-
808 out of Kir4.1 leads to glial membrane depolarization, inhibition of potassium and
809 glutamate uptake, and enhanced short-term synaptic potentiation. *J. Neurosci.* **27**,
810 11354–11365 (2007). DOI: 10.1523/jneurosci.0723-07.2007

811 45. Tong, X., Ao, Y., Faas, G. C., Nwaobi, S. E., Xu, J., Haustein, M. D., Anderson, M. A.,
812 Mody, I., Olsen, M. L., Sofroniew, M. V. & Khakh, B. S. Astrocyte Kir4.1 ion channel
813 deficits contribute to neuronal dysfunction in Huntington's disease model mice. *Nat.*
814 *Neurosci.* **17**, 694–703 (2014). DOI: 10.1038/nn.3691

815 46. Sofroniew, M. V. Astrocyte barriers to neurotoxic inflammation. *Nat. Rev. Neurosci.* **16**,
816 249–263 (2015). DOI: 10.1038/nrn3898

817 47. Álvarez-Buylla, A. & Ihrie, R. A. Sonic hedgehog signaling in the postnatal brain.
818 *Seminars in Cell and Developmental Biology* **33**, 105–111 (2014). DOI:
819 10.1016/j.semcdb.2014.05.008

820 48. Amankulor, N. M., Hambardzumyan, D., Pyonteck, S. M., Becher, O. J., Joyce, J. A. &
821 Holland, E. C. Sonic Hedgehog Pathway Activation Is Induced by Acute Brain Injury and
822 Regulated by Injury-Related Inflammation. *J. Neurosci.* **29**, 10299–10308 (2009). DOI:
823 10.1523/jneurosci.2500-09.2009

824 49. Sirko, S. et al. Reactive glia in the injured brain acquire stem cell properties in response
825 to sonic hedgehog. [corrected]. *Cell Stem Cell* **12**, 426–39 (2013). DOI:
826 10.1016/j.stem.2013.01.019

827 50. Choe, Y., Huynh, T. & Pleasure, S. J. Epithelial cells supply Sonic Hedgehog to the
828 perinatal dentate gyrus via transport by platelets. *Elife* **4**, (2015). DOI:
829 10.7554/elife.07834

830 51. Bayraktar, O. A. et al. Single-cell in situ transcriptomic map of astrocyte cortical layer
831 diversity. *bioRxiv* 432104 (2018). DOI: 10.1101/432104

832 52. Miller, S. J. et al. Molecularly defined cortical astroglia subpopulation modulates neurons
833 via secretion of Norrin. *Nat. Neurosci.* **22**, 741–752 (2019). DOI: 10.1038/s41593-019-
834 0366-7

835 53. Sibille, J., Pannasch, U. & Rouach, N. Astroglial potassium clearance contributes to

836 short-term plasticity of synaptically evoked currents at the tripartite synapse. *J. Physiol.*
837 **592**, 87–102 (2014). DOI: 10.1113/jphysiol.2013.261735

838 54. Yang, G., Pan, F. & Gan, W.-B. Stably maintained dendritic spines are associated with
839 lifelong memories. *Nature* **462**, 920–924 (2009). DOI: 10.1038/nature08577

840 55. Madisen, L., Zwingman, T. A., Sunkin, S. M., Oh, S. W., Zariwala, H. A., Gu, H., Ng, L. L.,
841 Palmiter, R. D., Hawrylycz, M. J., Jones, A. R., Lein, E. S. & Zeng, H. A robust and high-
842 throughput Cre reporting and characterization system for the whole mouse brain. *Nat.*
843 *Neurosci.* **13**, 133–40 (2010). DOI: 10.1038/nn.2467

844 56. Long, F., Zhang, X. M., Karp, S., Yang, Y. & McMahon, A. P. Genetic manipulation of
845 hedgehog signaling in the endochondral skeleton reveals a direct role in the regulation of
846 chondrocyte proliferation. *Development* **128**, 5099–108 (2001). DOI: 10.1016/s0092-
847 8674(00)80094-x

848 57. Tsien, J. Z., Chen, D. F., Gerber, D., Tom, C., Mercer, E. H., Anderson, D. J., Mayford,
849 M., Kandel, E. R. & Tonegawa, S. Subregion- and cell type-restricted gene knockout in
850 mouse brain. *Cell* **87**, 1317–1326 (1996). DOI: 10.1016/S0092-8674(00)81826-7

851

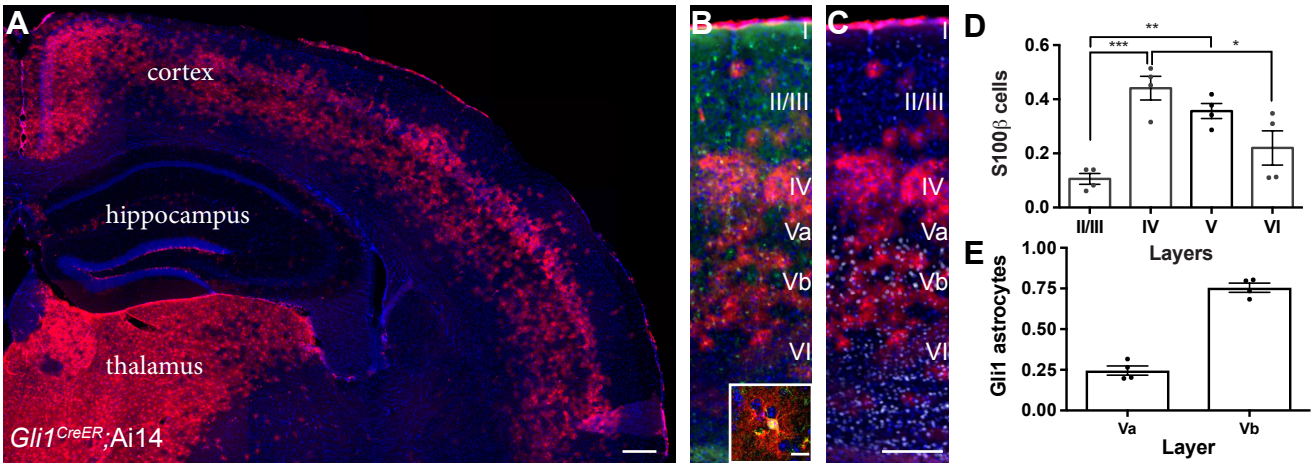

Figure 1: Gli1 astrocytes are distributed in a laminar-specific manner. (A) Tamoxifen-induced reporter expression in *Gli1*^{CreER};Ai14 mice reveals a laminar distribution of cells undergoing active Shh signaling (red). Scale bar, 250 μm. **(B)** Gli1+ cells (red) are a subset of all astrocytes (S100β, green, see inset; scale bar, 12.5 μm). **(C)** Layer analysis of Gli1 astrocytes (red) with DAPI and the deep layer marker Ctip2 (gray) illustrate their layer-specific organization. Scale bar, 125 μm. **(D)** The fraction of astrocytes expressing Gli1 in each cortical layer. Data points indicate individual animals, bars represent mean ± SEM. Statistical signficance was assessed by one-way ANOVA with Tukey's post hoc test for multiple comparisons. *, $p < 0.05$; **, $p < 0.01$; ***, $p < 0.01$. **(E)** The fraction of Gli1 astrocytes in sublayers Va and Vb. Bar graphs represent mean value ± SEM. $n = 4$ animals.

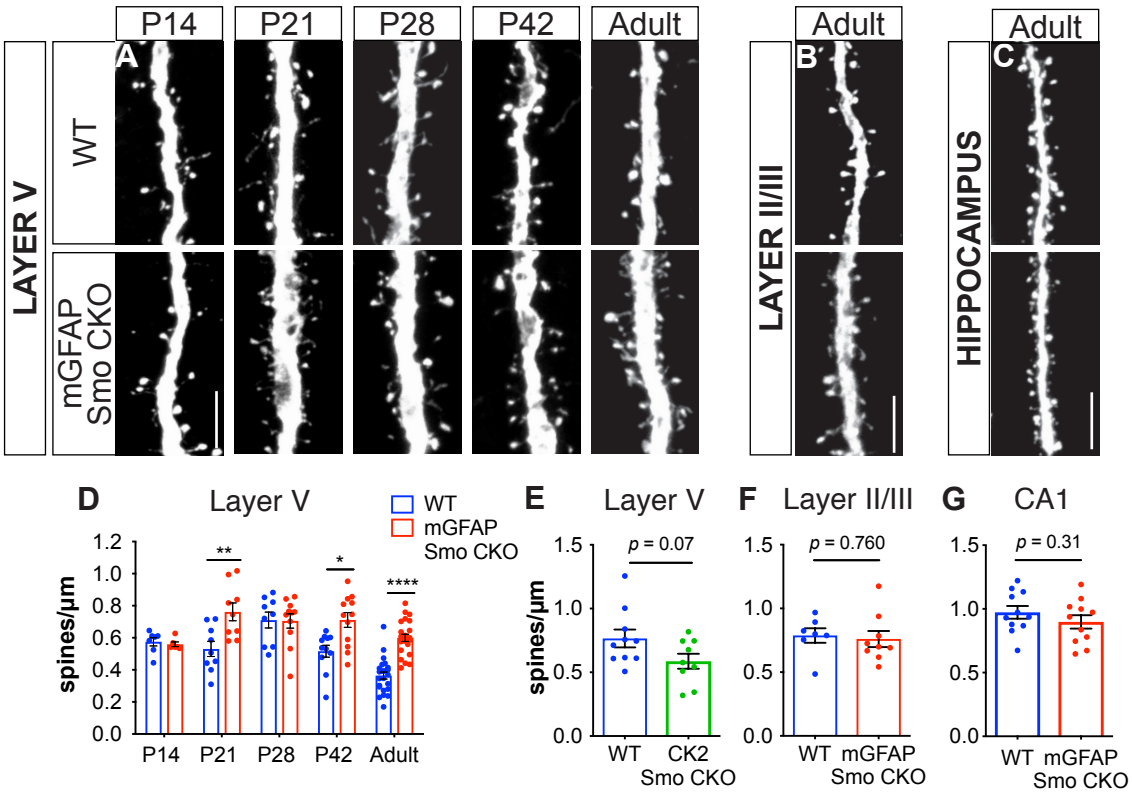

Figure 2: Loss of Shh signaling in astrocytes results in increased spine density on layer V neurons. (A) GFP immunostaining of representative apical dendritic segments from layer V neurons in WT and mGfap Smo CKO mice at all ages and regions analyzed. Scale bar, 5 μm. (**D**) Spine density of apical dendrites from layer V neurons across various postnatal ages and in adult mice. Data points represent individual cells, bars represent mean ± SEM. Statistical analysis performed by two-way ANOVA with Tukey's post-hoc test for multiple comparisons. *, $p < 0.05$; **, $p < 0.01$; ****, $p < 0.0001$. Significance is stated as mGFAP Smo CKO compared to WT at a given age. (**E**) Spine density of apical dendrites from layer V neurons in adult CamKIIa Smo CKO mice. (**F-G**) Spine density of apical dendrites from layer II/III (F) and CA1 pyramidal neurons (G) in WT and mGfap Smo CKO mice. Data points represent individual cells, bars represent mean ± SEM. Statistical signficance assessed by Student's t-test. $n \geq 3$ animals per genotype for all ages except P14, where $n = 2$ animals per genotype.

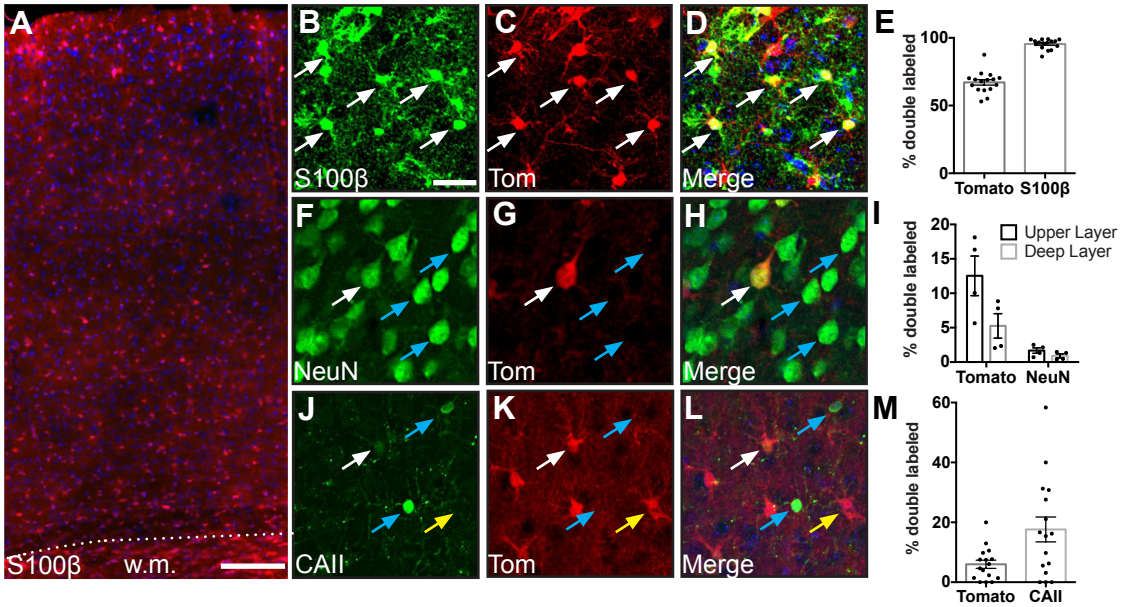

Figure 2 – figure supplement 1: mGfap-Cre recombination occurs primarily in astrocytes. (A) Representative image of tdTomato expression in the cortex of *mGfap-Cre;*Ai14 mice. w.m., white matter. Scale bar, 125 μm. **(B-D)** Expression of the astrocyte marker S100β and tdTomato in somatosensory cortex. Scale bar, 25 μm. **(E)** Fraction of recombined cells identified as astrocytes in the cortex of adult *mGfap-Cre;*Ai14 mice. **(F-H)** Expression of the neuronal marker NeuN and tdTomato in somatosensory cortex. **(I)** Fraction of recombined cells identified as neurons. **(J-L)** Expression of the oligodendrocyte marker CAII and tdTomato in somatosensory cortex. **(M)** Fraction of recombined cells identified as oligodendrocytes. White arrows show double-labeled cells, blue arrows show cells that express the indicated marker but are tomato-negative, and yellow arrows show single-labeled tomato-positive cells. Data points represent individual brain sections analyzed. Bar graphs represent mean ± SEM. *n* = 2 animals, four sections per animal.

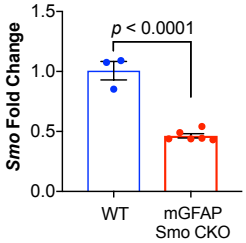

Figure 2 - figure supplement 2: mGFAP Smo CKO mice have reduced levels of *Smo*. Quantitative PCR of cortical RNA shows a significant reduction in *Smo* expression. Data points represent individual animals, bars represent mean ± SEM. Statistical analysis assessed by unpaired Student's t-test.

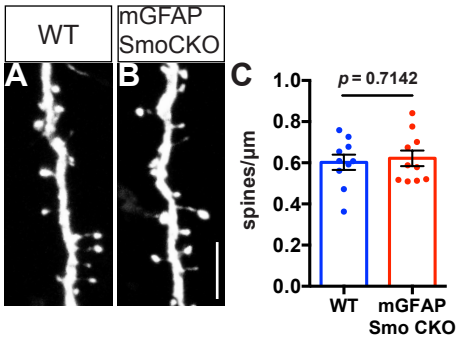

Figure 2 – figure supplement 3: Spine density on layer V basal dendrites are not affected in adult mGFAP Smo CKO mice. **(A-B)** Representative images of basal dendrites analyzed from layer V neurons expressing *Thy1GFPm* in both WT (*Smo*$^{fl/fl}$) and mGFAP Smo CKO (*mGfap-Smo*$^{fl/fl}$) animals. Scale bar, 5 µm. **(C)** Graph comparing the density of spines on basal dendrites from WT and mGFAP Smo CKO animals. Data points represent individual cells, bars represent mean ± SEM. Statistical significance was assessed using unpaired Student's t-test. *n* = 3 animals per genotype.

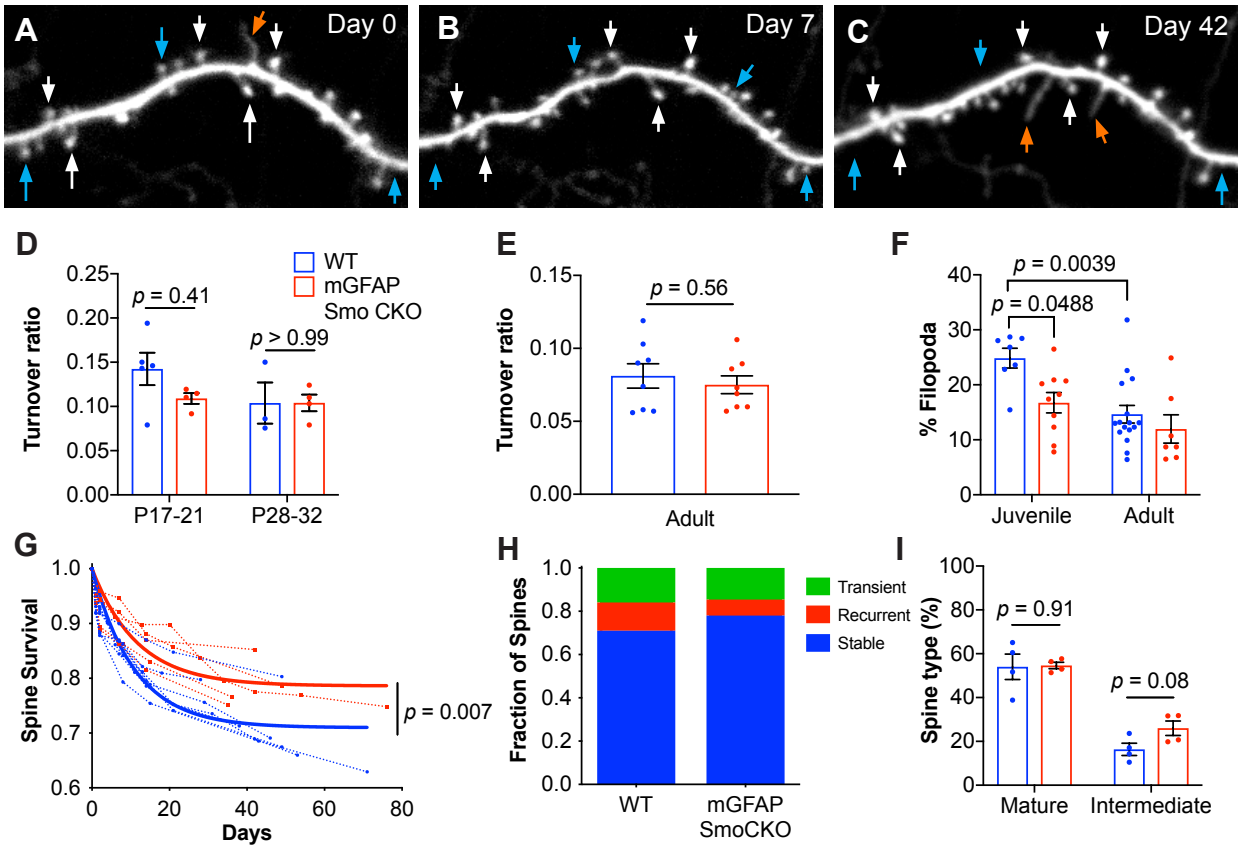

Figure 3: Loss of astrocytic Shh signaling impairs structural plasticity. (**A-C**) Example dendrite segment imaged repeatedly over 6 weeks. Day 0 indicates the first day of imaging, subsequent imaging days indicated. White arrows, stable spines; cyan arrows, transient spines; orange arrows, filopodia. (**D**) Turnover ratios in WT (n = 3-5 animals per age group) and mGFAP Smo CKO juvenile mice (n = 4 animals per age group) analyzed over 2 days. **(E)** Turnover ratios in WT (n = 8 animals) and mGFAP Smo CKO (n = 8 animals) adult mice analyzed over 7 days. Statistical analysis by two-way ANOVA, Tukey's post hoc test (D) and unpaired Student's t-test (E). (**F**) Fraction of protrusions identified as filopodia in juvenile (WT, n = 7 animals; mGFAP Smo CKO, n = 10 animals) and adult mice (WT, n = 16: mGFAP Smo CKO, n = 7 animals). Statistics by two-way ANOVA, Tukey's post hoc test. (**G**) Comparison of spine survival curves for WT and mGFAP Smo CKO neurons. Each dashed curve represents the curve from an individual mouse (WT, n = 7 animals; mGFAP Smo CKO, n = 5 animals). Solid curves represent best-fits to exponential decay models. (**H**) The fraction of spines belonging to the stable, recurrent, and transient populations. Statistical significance was assessed by Student's t-test for each class (stable, recurrent, or transient; n = 7 and 8 animals, WT and mGFAP Smo CKO, respectively). Stable, p = 0.0485; Recurrent, p = 0.1023; Transient, p = 0.7709. **(I)** Breakdown of spine morphology in juvenile mice. Statistical analysis by unpaired Student's t-test for each spine class. For graphs D-F and I, data points represent individual animals, bars represent mean ± SEM.

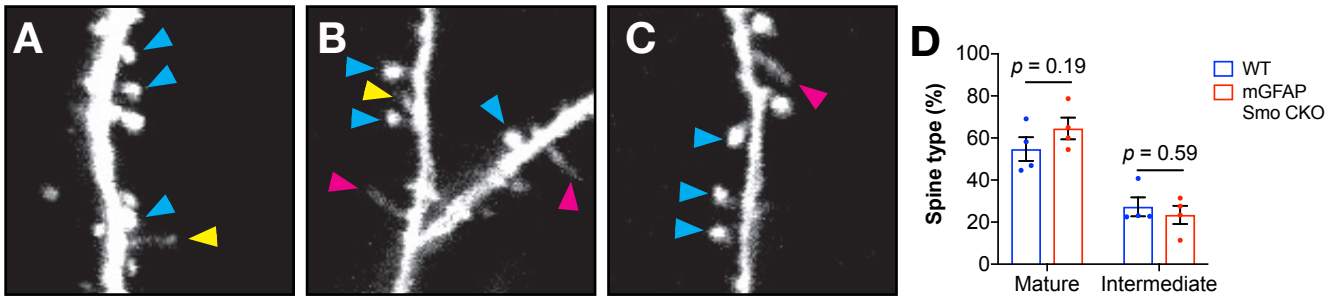

Figure 3 - Supplement 1. (**A-C**) Several examples of protrusions classified as mushroom (blue arrowheads) or intermediate (yellow arrowheads) spines, and filopodia (pink arrowheads). Note the thin stalk and small bulbous head of the intermediate spine in A, whereas filopodia lack a discerible head (B and C). (**D**) The fraction of protrusions classified as mushroom or intermediate in adult mGFAP Smo mice and WT controls. Data points represent individual animals, bars represent mean ± SEM. Statistical analysis by unpaired Student's t-test.

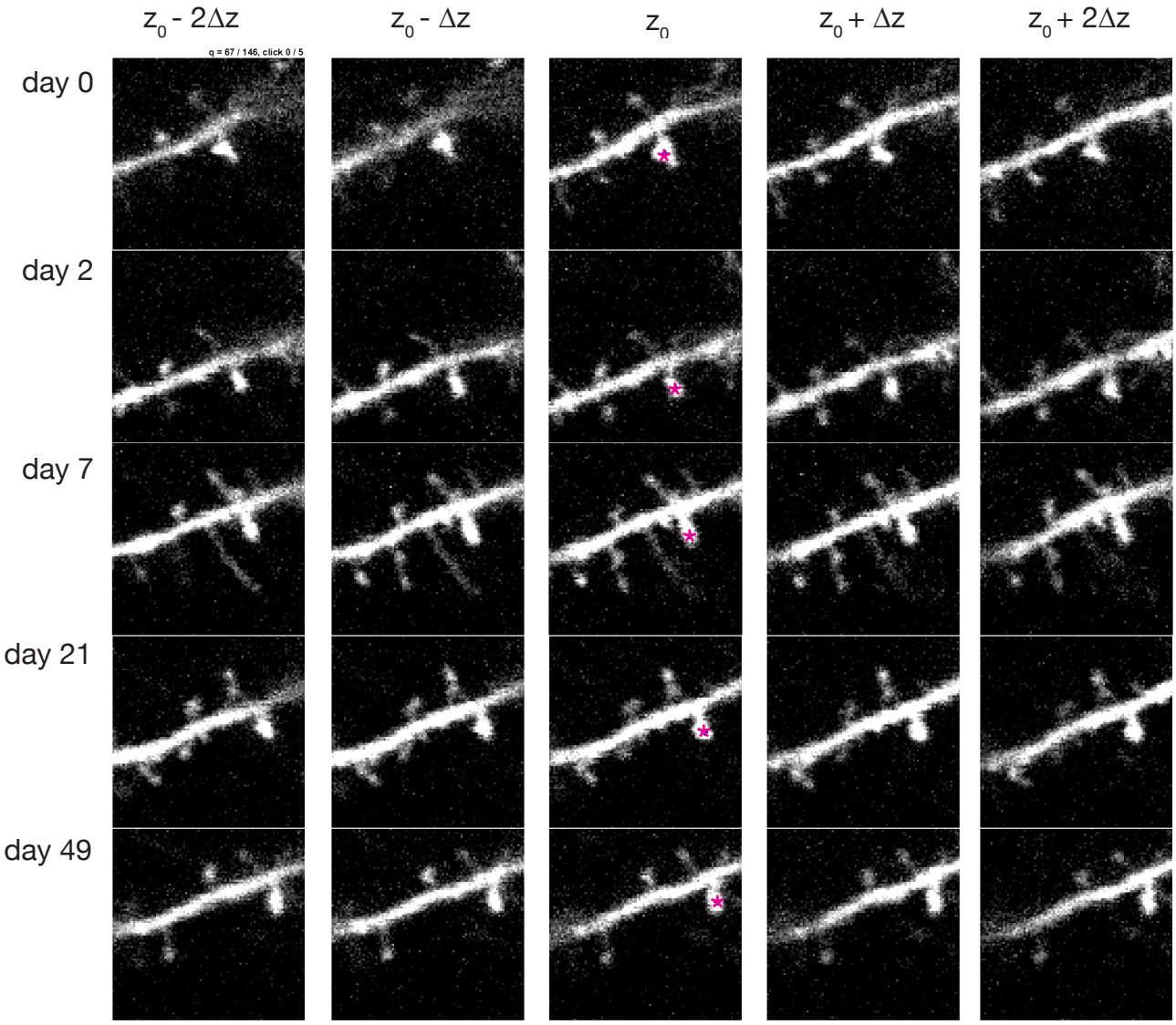

Figure 3 - Supplement 2. Screenshot depicting the graphical user interface used for longitudinal tracking of spines across multiple days of imaging. A spine identified in the first imaging session (pink star, top central panel) is presented to the user for scoring. The same spine is manually tracked across subsequent days (rows). For each day, multiple frames above and below the estimated z-plane corresponding to that spine, Z0, are also presented (columns). For each timepoint, the user then clicks on the spine's head using the frame that best captures the spine. In this case, the frame jump, Δz, was set to 1, and 4 neighboring frames are presented; these parameters can be adjusted as necessary.

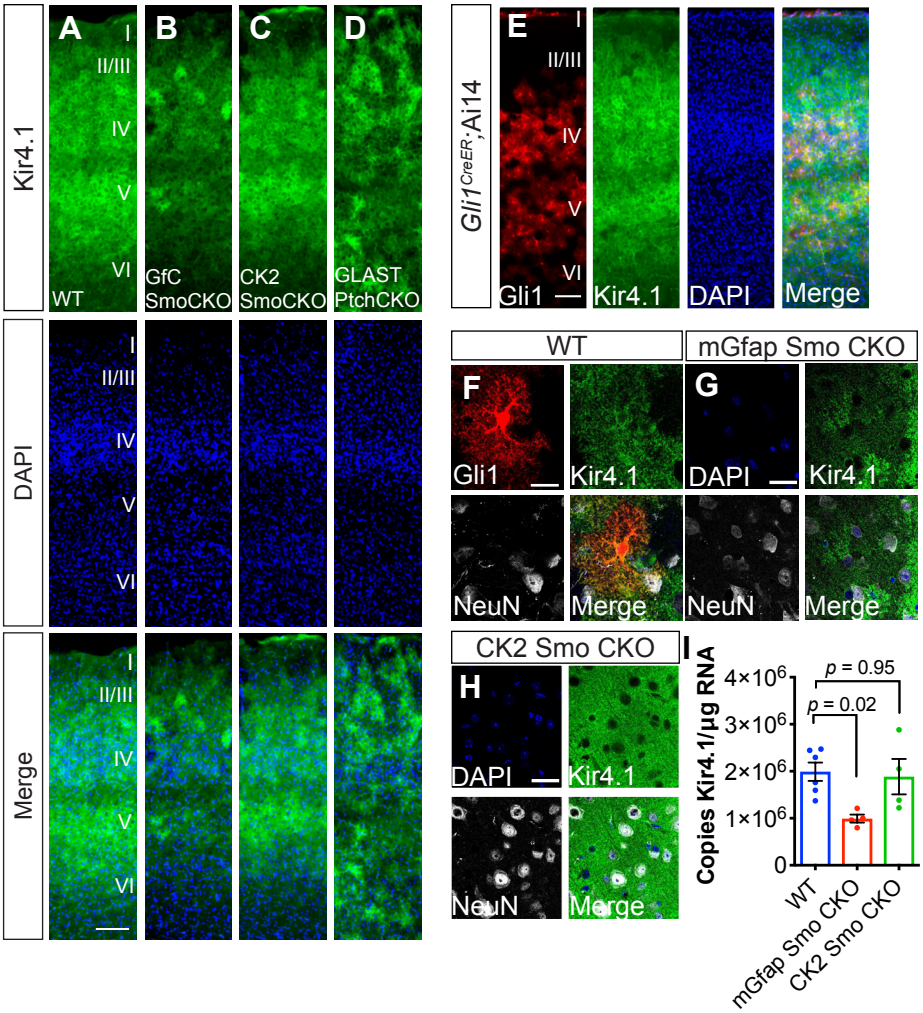

Figure 4: Shh signaling regulates Kir4.1 expression in the cortex. (A-D) Immunofluorescence for Kir4.1 in the cortex of adult WT (A), mGfap Smo CKO (B), CK2 Smo CKO (C) and GLAST Ptch CKO mice (D). Scale bar, 125 µm. **(E)** Fluorescence micrographs showing the distribution of Gli1 astrocytes (red) and Kir4.1 (green) in the cortex of an adult *Gli1Cre*^{ER};Ai14 mouse counterstained with DAPI (blue). **(F-G)** Confocal images of Gli1 (F, red) Kir4.1 (green) and NeuN (white) from adult WT (F), mGfap SmoCKO (G), or CamK2a SmoCKO (H) mice. Scale bar, 25 µm. **(I)** Gene expression levels in the cortex of Kir4.1 from WT (n = 6 animals) and mGfap Smo CKO or CK2 Smo CKO mice (n = 4 each). Data points represent individual animals and bar graphs represent mean value ± SEM. Statistical significance was assessed by one-way ANOVA with Tukey's test for multiple comparisons. Significance stated on the graph is compared to WT.

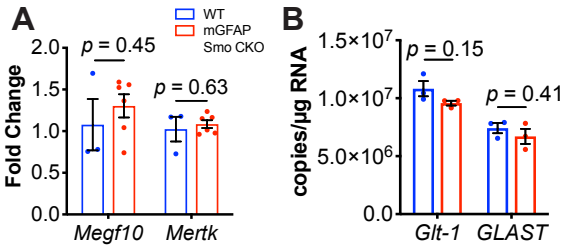

Figure 4 – figure supplement 1: Quantititive PCR analysis of known spine and synapse modulators show no change in expression in mGFAP Smo CKO mice. (A) Quantitive PCR shows no change in *Megf10* or *Mertk* in mGFAP Smo CKO animals compared to controls (n = 3 and 6 samples of cortical RNA from WT and mGFAP Smo CKO animals, respectively). Statitistical significance assessed by unpaired Student's t-test of the quantification cycles for each sample. Error bars represent standard error of the mean. **(B)** Droplet digital PCR shows no difference in the number of trancripts of either *GLT-1* or *GLAST* in mGFAP Smo CKO animals (n = 3 cortical RNA samples per genotype). Statistical significance assessed by unpaired Student's t-test of the copy number for each target in each genotype. Error bars represent standard error of the mean.

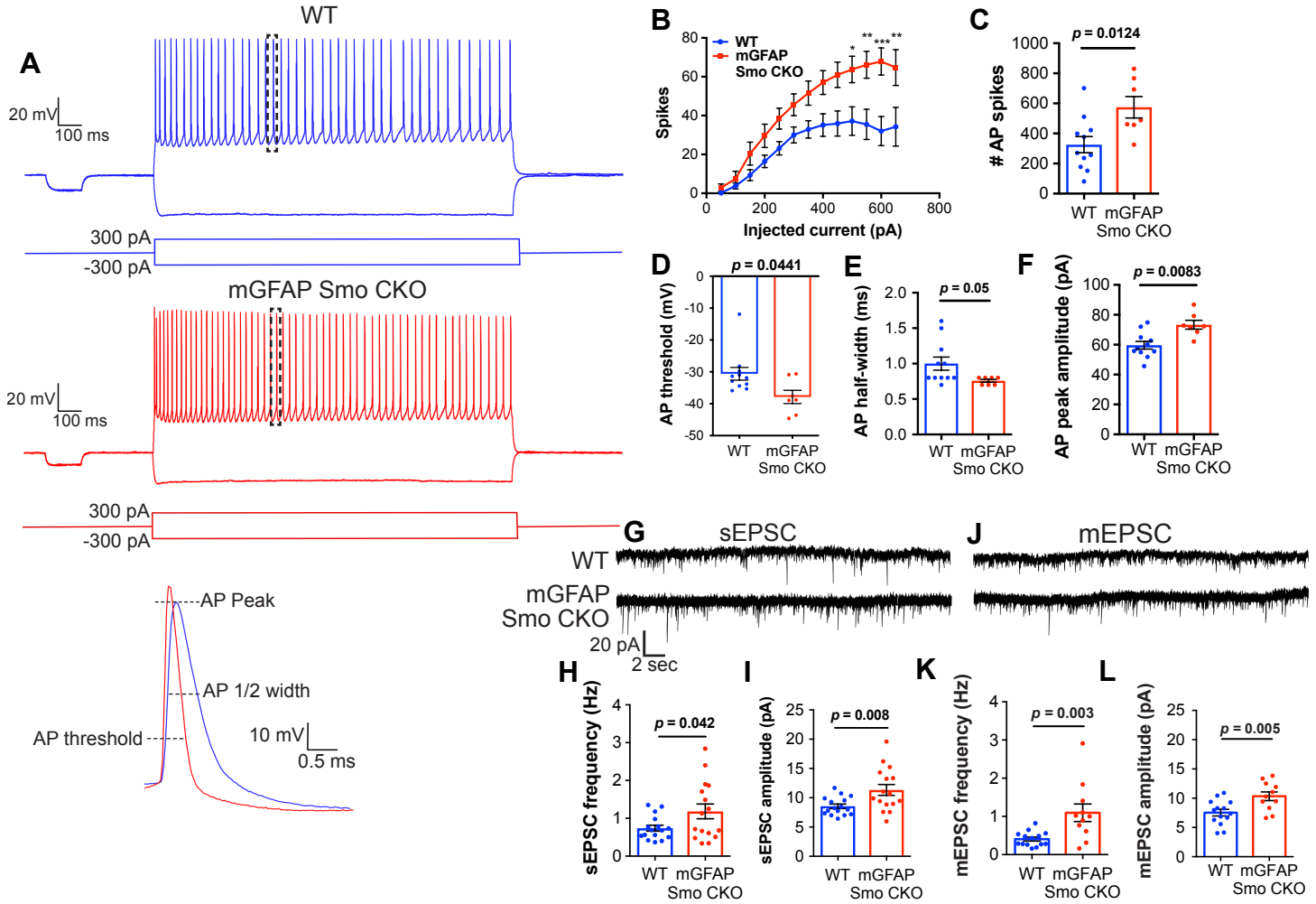

Figure 5: Neurons in mGFAP Smo CKO mice exhibit a significant increase in excitability and synaptic transmission. (A) Example traces of action potentials from layer V pyramidal neurons in WT and mGFAP Smo CKO mice at P21. Samples of action potential spikes (dashed lines, lower panel) describe AP threshold, AP peak amplitude, and AP ½ width of pyramidal neurons. **(B)** Line graph displays relationship between action potential spike numbers (y-axis) and current injection; mGFAP Smo CKO neurons exhibit an increase in AP spikes (>500 pA) compared to WT neurons. Statistical signifcance was assessed by two-way ANOVA with Sidak's test for multiple comparisons and stated as mGFAP Smo CKO compared to WT at a given current (n = 11 and 7 cells from WT and mGFAP Smo CKO, respectively). **(C-F)** Bar graphs describe an increase in total AP spike numbers (C), reduction in AP threshold (mV) (D), reduction in AP 1/2 width (E), and increase in AP peak amplitude (pA) (F) in mGFAP Smo CKO neurons. **(G)** Example traces of sEPSCs from layer V pyramidal neurons recorded in the presence of picrotoxin from WT and mGFAP Smo CKO mice at P21. **(H-I)** Summary graphs of sEPSC frequency and amplitude (n = 14 and 11 cells from WT and mGFAP Smo CKO animals, respectively). **(J)** Example traces of mEPSCs from layer V pyramidal neurons recorded in the presence of picrotoxin and TTX. **(K-L)** Summary graphs of mEPSC frequency and amplitude (n = 16 cells per genotype). mGFAP Smo CKO neurons exhibit increases in both frequency and amplitude in sEPSCs and mEPSCs recordings. Statistical significance was assessed by unpaired Student's t-test. For each graph, data points represent individual cells. All data are from at least 3 animals per genotype.

	WT (n = 11 cells)	mGFAP Smo CKO (n = 7 cells)	*P* value
Input resistance (MΩ)	130.6 ± 21.52	97.93 ± 11.49	0.15
Resting membrane potential (mV)	-59.37 ± 2.059	-63.73 ± 3.248	0.25
Tau (ms)	11.76 ± 0.71	11.75 ± 1.398	0.79

Figure 5 – figure supplement 1. Membrane properties of mGFAP Smo CKO layer V pyramidal neurons. There is a significant decrease in input resistance (MΩ) in mGFAP Smo CKO neurons compared to WT neurons. No significant differences were observed in resting membrane potential (mV), rheobase (pA), and tau (ms) in mGFAP Smo CKO neurons. Statistical significance was assessed by Mann-Whitney U test (input resistance and tau) and unpaired Student's t-test (resting membrane potential).

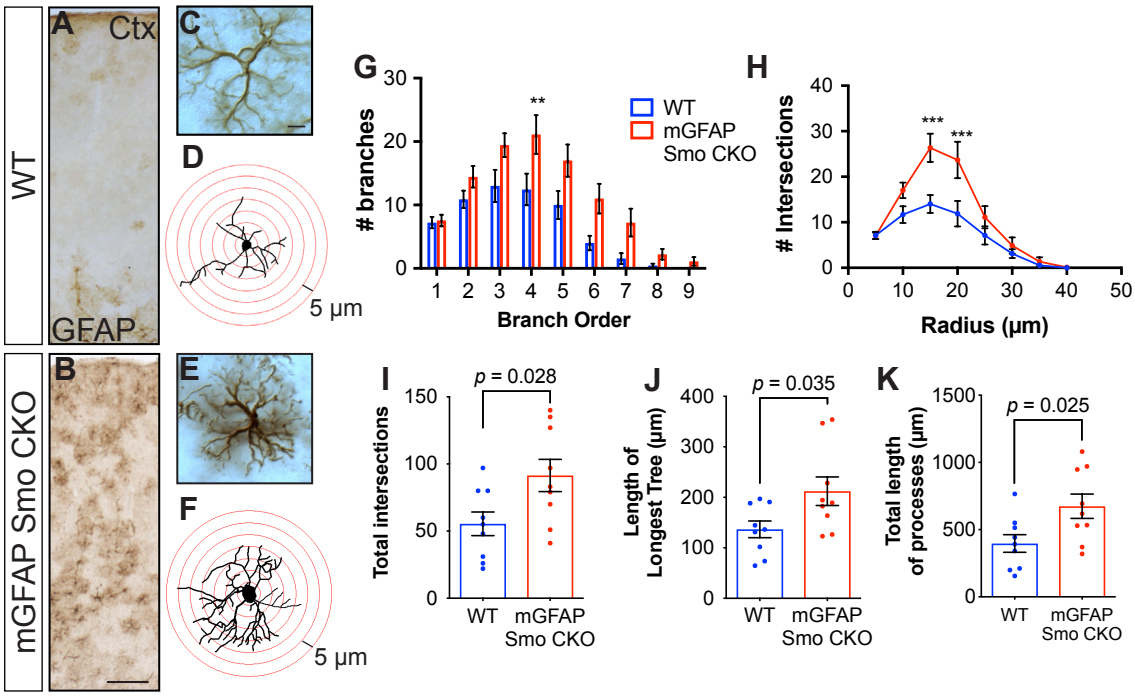

Figure 6: Disruption of Shh signaling in astrocytes results in widespread reactive changes in morphology. (A-B) Brightfield immunohistochemistry reveals a reactive upregulation of GFAP across cortical layers in mGFAP Smo CKO astrocytes. Scale bar, 125 µm. **(C & E)** Representative high-magnification images of both WT (C) and mGFAP Smo CKO (E) astrocytes are shown. Scale bar, 10 µm. **(D & F)** Representative traces of GFAP expression from WT (D) and mGFAP Smo CKO (F) cortical astrocytes. **(G & H)** Sholl analysis shows significant increases in complexity of mGFAP Smo CKO astrocytes compared to WT controls. Statistical significance was assessed by one-way ANOVA with Bonferroni's for multiple comparisons. **(I-K)** Quantification of various morphological features of traced astrocytes. Statistical analysis performed by one-way ANOVA (G & H) and unpaired Student's t-test (I-K). Data points represent individual cells. Graphs represent mean value ± SEM. *n* = 3 animals per genotype.

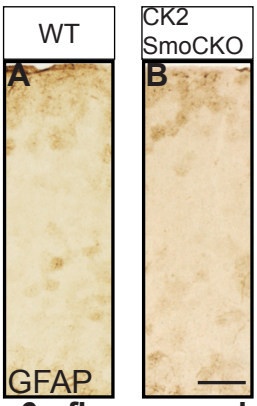

Figure 6 – figure supplement 1: Reactive gliosis does not occur when neuronal Shh signaling is disrupted. Brightfield immunohistochemistry for GFAP in the cortex of an adult *CamKIIa;Smo*$^{fl/fl}$ animal (B) and littermate control (A) shows comparable levels of GFAP expression. Scale bar, 125 μm.